Electronic Supplementary Material (ESI) for Dalton Transactions.
This journal is © The Royal Society of Chemistry 2021

Thermo- and Photo-Induced Spin State Switching in an Iron(II) 2D Coordination Network associated with Large Light-Induced Thermal Hysteresis and Tuning of Dimensionality via Ligand Modulation

Subrata Ghosh,[a] Sujit Kamilya,[a] Titas Pramanik,[a] Ashutosh Mohanty,[a] Mathieu Rouzières,[b] and Radovan Herchel,[c] Sakshi Mehta,[a] Abhishake Mondal*[a]

[a]Solid State and Structural Chemistry Unit, Indian Institute of Science, Sir C. V. Raman Road, Bangalore 560012, India. Email: mondal@iisc.ac.in, http://m2sscuiisc.in/.

[b]Univ. Bordeaux, CNRS, Centre de Recherche Paul Pascal, CRPP, UMR 5031, 33600 Pessac, France.

[c]Department of Inorganic Chemistry, Faculty of Science, Palacký University, CZ-771 46 Olomouc, Czech Republic.

Correspondence to: mondal@iisc.ac.in

Table of Contents

Materials 7

Synthesis of **L1** 7

Physical measurements 7

Magnetic measurements 8

X-ray crystallography 9

Optical reflectivity measurements 10

Photoluminescence Measurements 11

Figures 13

Tables 61

Fig. S1. ^{1}H NMR ($CDCl_3$, 500 MHz) spectrum of **L1** 13

Fig. S2. ^{13}C NMR ($CDCl_3$, 125 MHz) spectrum of **L1** 13

Fig. S3. Thermogravimetric analysis (TGA) curves for **1** - **3** from 30 to 600°C at a 10 °C min^{-1} temperature rate under N_2 atmosphere. 14

Fig. S4. Comparison of the room temperature experimental PXRD pattern and the 120 K simulated one for **1**. 14

Fig. S5. Comparison of the room temperature experimental PXRD pattern and the 120 K simulated one for **2**. 15

Fig. S6. Comparison of the room temperature experimental PXRD pattern and the 200 K simulated one for **3**. 15

Fig. S7. IR spectra of ligands **L1** and **L2** with complexes **1** - **3** at RT. 17

Fig. S8. UV-vis spectra of **L1** and **L2** in DCM at room temperature. 17

Fig. S9. UV-vis-NIR spectra of **1** and **2** in MeOH with dilute (left) and concentrated (right) solutions at room temperature. 18

Fig. S10. Solid state UV-vis-NIR spectra of **1** - **3** at room temperature. 18

Fig. S11. Cyclic voltammograms of the ligand **L1** in DCM containing 0.1 M ($^{n}Bu_4N)PF_6$ at room temperature with a scan rate of 0.1 V/s. Arrows indicate the open circuit potential with the direction of the potential sweep 19

Fig. S12. Cyclic voltammograms for the oxidation (left) and reduction (right) of **1** in MeOH/DCM containing 0.1 M (^{n}Bu$_4$N)PF$_6$ with a scan rate of 0.1 V/s at room temperature. Arrows indicate the open circuit potential with the direction of the potential sweep. 20
Fig. S13. Square wave voltammograms of **1** in MeOH/DCM containing 0.1 M (^{n}Bu$_4$N)PF$_6$ at room temperature. Arrows indicate the open circuit potential with the direction of the potential sweep. 20
Fig. S14. Cyclic voltammograms for the oxidation (left) with various scan rates and reduction (right) of **2** in MeOH/DCM containing 0.1 M (^{n}Bu$_4$N)PF$_6$ with a scan rate of 0.1 V/s at room temperature. Arrows indicate the open circuit potential with the direction of the potential sweep. 21
Fig. S15. Square wave voltammograms of **2** in MeOH/DCM containing 0.1 M (^{n}Bu$_4$N)PF$_6$ at room temperature. Arrows indicate the open circuit potential with the direction of the potential sweep. 21
Fig. S16. Cyclic voltammograms of the reaction mixture of Fe(NCS)$_2$ and two equivalents of **L2** in DCM/MeOH (1:1) containing 0.1 M (^{n}Bu$_4$N)PF$_6$ at room temperature with a scan rate of 0.1 V/s, oxidation (left) and reduction (right). Arrows indicate the open circuit potential with the direction of the potential sweep. 22
Fig. S17. Square wave voltammograms of the reaction mixture of Fe(NCS)$_2$ and two equivalents of **L2** in DCM/MeOH (1:1) containing 0.1 M (^{n}Bu$_4$N)PF$_6$ at room temperature. Arrows indicate the open circuit potential with the direction of the potential sweep. 22
Fig. S18. Left: ORTEP view of asymmetric unit in **1**. Right: Unit cell diagram showing along *b*-axis in **1** at 120 K. Hydrogen atoms are omitted for clarity (Fe: green, C: gray, N: blue, O: red, S: orange, H: pink). .. 23
Fig. S19. Left: ORTEP view of asymmetric unit in **2**. Right: Unit cell diagram showing along *b*-axis in **2** at 120 K. Hydrogen atoms are omitted for clarity (Fe: green, C: gray, N: blue, O: red, S: orange, Se: brown, H: pink). 23
Fig. S20. A view of several weak supramolecular interactions presents between to lateral 1D chains in **1**. (Fe: green, C: gray, N: blue, O: red, S: orange; H: light pink). 24
Fig. S21. A view of several weak supramolecular interactions presents between to lateral 1D chains in **2**. (Fe: green, C: gray, N: blue, O: red, S: orange; Se: brown; H: light pink). 24
Figure S22. A view of 1D layer formed by several weak supramolecular interactions in **1** (Fe: green, C: gray, N: blue, O: red, S: orange; H: light pink). 25
Fig. S23. A view of 1D layer formed by several weak supramolecular interactions in **2**. (Fe: green, C: gray, N: blue, O: red, S: orange; Se: brown; H: light pink) 25

Fig. S24. Top: ORTEP view of asymmetric unit in **3** at 200 K (left) and 90 K (right). Bottom: Unit cell diagram showing void channels in **3** at 200 K (left) and 90 K (right). Hydrogen atoms are omitted for clarity (Fe: green, C: gray, N: blue, O: red, S: orange, H: pink). 26
Fig. S25. Comparison of Fe–N distances in 3 at 200 and 90 K. 26
Fig. S26. Representation of the grid dimensional changes for **3** associated with the temperature change. 27
Fig. S27. Field dependence of the magnetization as *M* vs *H* plots for **1** (top, left), **2** (top, right) and **3** (bottom) at 100 K. The red line represents the best fit. 27
Fig. S28. Temperature dependence of χT product for **1** and **2** at 1000 Oe. 28
Fig. S29. Temperature dependence of the χT product of complexes **1** (top) and **2** (bottom) measured at H = 1000 and 10000 Oe plotted in normal scale (left) and log scale (right). 29
Fig. S30. Field dependence of the magnetization as *M* vs *H* (left) and *M* vs *H/T* (right) plots for **1** at 1.85, 3, 5 and 8 K. The solid lines are guide for the eyes. 29
Fig. S31. Field dependence of the magnetization as *M* vs *H* (left) and *M* vs *H/T* (right) plots for **2** at 1.85, 3, 5, and 8 K. The solid lines are guide for the eyes. 30
Fig. S32. Frequency vs temperature plot of the real (χ', left) and imaginary (χ'', right) components of the ac susceptibility at 0 Oe external dc field and different temperatures from 1.8 – 15 K (top) and different external dc field at 2 K (bottom), respectively with a 3 Oe ac field for a polycrystalline sample of **1**. 31
Fig. S33. Frequency vs temperature plot of the real (χ', left) and imaginary (χ'', right) components of the ac susceptibility at 0 Oe external dc field and different temperatures from 1.8 – 15 K (top) and different external dc field at 2 K (bottom), respectively with a 3 Oe ac field for a polycrystalline sample of **2**. 32
Fig. S34. Magnetic data for **1 - 2** showed as the temperature dependence of the χT product and the isothermal molar magnetization measured at *T* = 1.8, 3, 5, and 8 K in the inset. The empty symbols represent the experimental data; red full lines represent the fitted data using eqn (1) with spin Hamiltonian parameters listed in Table 2. 33
Fig. S35. The first derivative of χT against the temperature, dχT /dT *vs*. T, identifies $T_{1/2}$ = around 100 K for **3**. 33
Fig. S36. Temperature dependence of the χT product of complex **3** in heating and cooling modes at 1000 Oe. 34
Fig. S37. χT *vs.* T data of complex **3** fit using the ideal solution model. 35
Fig. S38. Field dependence of the magnetization as *M* vs *H* (left) and *M* vs *H/T* (right) plots for **3** at 1.85, 3, 5 and 8 K. The solid lines are guide for the eyes. 36

Fig. S39. Frequency (100 Hz) vs temperature plot of the real (χ', left) and imaginary (χ'', right) components of the ac susceptibility at 0 Oe external dc field and different temperatures from 1.8 – 15 K, respectively with a 3 Oe ac field for a polycrystalline sample of **3**. 36
Fig. S40. Selected optical reflectivity spectra between 270 and 10 K recorded in the dark in cooling (top, left) and heating (top, right) mode and at a scan rate of 4 K min^{-1} for **3**. Bottom: thermal evolution of absolute reflectivity signal plotted at 600 nm in cooling mode (270 - 10 K, at 4 K min^{-1}, blue circle markers) and heating mode (10 - 270 K, at 4 K min^{-1}, red circle markers) in dark. A spectroscopic white light of 0.5 mW/cm² has been used for these measurements. 37
Fig. S41. Variation of the absolute optical reflectivity (ΔAR) plotted at 600 nm and 10 K (after a fast cooling of the sample from room temperature) before and after excitation with different LEDs (10 min, at 16 mW cm^{-2}) for **3**. 38
Fig. S42. Comparison of optical reflectivity spectra at 270 K (red), 10 K (blue) in dark and after 10 min of successive 590 nm (16 mW cm^{-2}) excitation (green) for **3**..... 39
Fig. S43. Thermal evolution of reflectivity signal plotted at 600 nm during 590 nm irradiation (16 $mWcm^{-2}$, at 10 K) and in heating mode in dark (10-270 K, at 4 K/min, circle markers) for **3**. 39
Fig. S44. Left: Time evolution of reflectivity signal plotted at 600 nm during ON and OFF of the irradiation at 590 nm (16 mW/cm^2) for **3**. A weak time relaxation of the photo-excitation that can be seen mainly the first 5 minutes, is then very slow, with a loss after 30 minutes of dR = 0.002 a.u. (for a photo-induced modification of 0.028 a.u.); Right: Time evolution of reflectivity signal plotted at 600 nm during the irradiation at 590 nm with different power for **3**. 40
Fig. S45. Variation of the absolute optical reflectivity (ΔAR) plotted at 600 nm and 10 K, after first irradiation 590 nm LED (30 min, 16 mW cm^{-2} with successive second excitation with different LEDs (10 min, 16 mW cm^{-2}) for **3**..... 40
Fig. S46. Comparison of the surface-reflectivity spectra at 10 K (reached from 270 K at 4 K min^{-1} in the dark; blue) and after 10 min of successive 590 nm (16 mW cm^{-2}) (green) and 850 nm (120 $mWcm^{-2}$) (red) excitation for **3**. 41
Fig. S47. Thermal evolution of reflectivity signal plotted at 600 nm after 850 nm irradiation (120 $mWcm^{-2}$, at 10 K, green circle markers) and in heating mode in dark (10-270 K, at 0.4 K/min, red circle markers) for **3**. Arrow indicates decreased in reflectivity during 850 nm irradiation. 41
Fig. S48. χT *vs* time curves for **3** under 405, 532, 650, and 808 nm laser light irradiations at 10 K and 10000 Oe field. 42
Fig. S49. χT *vs* time curves for **3** under 650 nm laser light irradiations at 10 K and 10000 Oe field. 42

Fig. S50. M *vs* H curves of **3** after 650 nm light irradiation (red) and in dark (black) at 2 K. 43
Fig. S51. Frequency dependency of the real (χ', left) and imaginary (χ'', right) components of the ac susceptibility under applied external dc field at 1.9 K with a 3 Oe ac field for a polycrystalline sample of **3** after 650 nm light irradiation..... 43
Fig. S52. χT *vs* time curves for **3** under 650 nm laser light irradiations at 10 K and 10000 Oe field during ON and OFF modes. 44
Fig. S53. χT *vs* T curves of **3** under continuous 650 nm light irradiation in heating and cooling modes with a sweep rate of 0.4 K min^{-1} at 10000 Oe field. 44
Fig. S54. Luminescence spectra of **L1** and **L2** at room temperature. 45
Fig. S55. Luminescence spectra of **1** - **3** at room temperature..... 45
Fig. S56.Temperature dependence luminescence spectra of **3**. 46
Fig. S57. The results of CASSCF/DLPNO-NEVPT2 for [Fe(**L1**)$_2$(NCS)$_2$(MeOH)$_2$] of **1**, [Fe(**L1**)$_2$(NCSe)$_2$(MeOH)$_2$] of **2** and [Fe(**L2**)$_4$(NCS)$_2$] of **3**. Left: the splitting of d-orbitals resulting from AILFT analysis; middle: the ligand field terms (LFT); right: the ligand field multiplets (LFM). 46
Fig. S58. Fig. 15 Left: the TD-DFT calculated absorption spectrum of HS and LS spin isomers of **3**, [Fe(**L2**)$_4$(NCSe)$_2$] calculated with B3LYP functional. Right: selected Natural Transition Orbitals (NTO) for transition I.^{LS} and III.^{HS}, while all NTOs are depicted in Fig. S59..... 47
Fig. S59. The Natural Transition Orbitals (NTO) calculated for LS and HS isomers of [Fe(**L2**)$_4$(NCS)$_2$] of **3** with TD-DFT using B3LYP functional on optimized molecular geometries..... 48

Table S1. X-ray crystallography data for complexes **1** - **3**..... 61
Table S2. Selected bond lengths and angles for **1** and **2** at 120 K. 62
Table S3. CShM analysis data for complexes **1** - **3**..... 63
Table S4 Selected hydrogen-bond parameters for **1** and **2** at 120 K..... 64
Table S5. Selected bond lengths and angles for **3** at 90 K and 200 K. 64

Experimental Section

Materials

All manipulations were carried out under an argon atmosphere using standard Schlenk techniques unless otherwise stated. Solvents were dried by standard methods and freshly distilled prior to use. All chemicals were used as purchased from chemical sources without further purification. The ligand **L2** was synthesized according to the literature procedure.[1]

Synthesis of L1

The ligand **L1** was prepared according to the literature procedure as yellow solid.[2] ^{1}H-NMR (500 MHz, $CDCl_3$): δ (ppm) = 8.59 (d, *J* = 6.3 Hz, 1H), 7.64 (d, *J* = 6.3 Hz, 1H), 7.26 (s, 1H), 4.45 (s, 1H). ^{13}C NMR (125 MHz, $CDCl_3$): δ (ppm) = 150.00 (CH), 141.53 (C), 139.91 (C), 120.09 (CH), 115.02 (C), 64.85 (CH_2). ATR-IR (only intensive bands): ν (cm^{-1}) = 2959, 2923, 1590, 1541, 1514, 1474, 1444, 1408, 1370, 1323, 1296, 1217, 1105, 1073, 1025, 990, 914, 850, 811, 794, 666, 648, 595, 536, 488 and 467. UV-vis (DCM, RT): λ_{max} (nm) (ε_M / M^{-1} cm^{-1}) 274 (4820), 347 (24700) and 361 (20831).

Physical measurements

The elemental analyses of C, H, and N were performed with Thermo Scientific Flash 2000 Organic Elemental Analyzer. The NMR spectra were recorded on the device ECZ500 from JEOL. The chemical shift is indicated by the δ scale in ppm. The signals of the residual protons (^{1}H) or carbons (^{13}C) atom in the deuterated solvents were used as the internal standard. The spectra were evaluated using the MestReNova program. Infrared (IR) spectra were recorded in the range of 4000 – 400 cm^{-1} on Bruker Tensor 27 spectrometer. UV/VIS/NIR spectra were carried out in the region of 250 – 2000 nm on a Lambda 750 UV/VIS/NIR spectrometer. Solid-state UV/VIS/NIR measurements were carried out by taking 5% sample by weight in KBr. Thermogravimetric analysis (TGA) was done on a Mettler Toledo TGA/SDTA851 analyzer with a heating rate of 10 °C min^{-1} under a nitrogen atmosphere ranging from 30°C to 300 °C. Powder X-ray diffraction (PXRD) measurements were carried out on a PANalytical Empyrean diffractometer at 45 kV and 30 mA, under Cu-Kα radiation (λ = 1.54059 Å). PXRD data analyses were done using PANalytical X'Pert HighScore Plus software. Electrochemistry studies were performed with a Metrohm

Autolab PGSTAT101 using platinum as a working electrode with 0.1 M ($^{n}Bu_4$)NPF_6 as a supporting electrolyte. The concentration of the sample used is around 1 mM. Ferrocene was used as an internal reference.

Magnetic measurements

The magnetic susceptibility measurements were performed with Quantum Design MPMS-XL SQUID magnetometer, between 1.85 K and 280 K for dc applied fields ranging from -7 to 7 T. Polycrystalline sample of **1** (12.19 mg), **1** (12.36 mg), and **3** (9.64 mg) introduced in a polyethylene bag (2.9 × 0.6 × 0.02 cm) were subjected to measurements. The temperature-dependent data were measured using 1000 Oe. The isothermal magnetization data were acquired at 1.85, 3, 5 and 8 K. *M vs H* measurements were performed at 100 K to check for the presence of ferromagnetic impurities which were found to be absent. The magnetic data were corrected for the sample holder and the diamagnetic contribution.

We have also performed the magnetic measurements keeping Crystals in Mother liquor. Crystals of all complexes were covered and thus restrained in a minimum amount of frozen mother liquor within a sealed straw to prevent their desolvation. No evaporation of the mother liquor was observed during the measurements. The mass of the sample was estimated after the measurements and after the mother liquor removal/evaporation

The *ac* susceptibility measurements were measured with an oscillating *ac* field of 3 Oe with frequency between 1 to 1500 Hz using MPMS-XL and from 10 to 10000 Hz using PPMS 9T.

(Photo)Magnetic measurements were carried out by using a sample holder inside the Quantum Design MPMS-XL EverCool SQUID magnetometer equipped with an optical fiber. In a typical experiment, 1.1 mg of finely ground crystals were deposited on an adhesive tape. The sample was separated from the end of the fiber by 6.5 cm. All the irradiations were carried out at 10 K to minimize the temperature variation induced by the light. The experimental data were corrected for the diamagnetic contribution of the constituent atoms as well as by the residual diamagnetic signal from the holder. Different

Laser sources were also used in the visible range in order to improve the photoinduced effect (ranging from 405 nm to 808 nm with powers of 12 - 5 mW/cm^2). Note that the temperatures have been corrected to consider the light irradiation heating (an average +1.5 K has been observed with 650 nm diode laser). Experimental susceptibilities were corrected for sample holder and intrinsic diamagnetic contributions.

X-ray crystallography

Single crystal X-ray structure analysis data of **1**, **2**, and **3** were collected on an Oxford Xcalibur Mova E diffractometer equipped with an EOS CCD detector, and a micro focus sealed tube using Mo-Kα radiation (λ =0.71073 Å). The single crystal was mounted on a crystal mounting loop with the help of Paratone oil at 240 K and slowly cooled down to the measured temperature with 2 K / min ramping rate using a liquid nitrogen gas-stream cooling device, followed by data collection at respective temperatures. Cell refinement, data integration, and reduction were carried out using the program CrysalisPro. Structures were solved using direct methods and refined with a full-matrix least-squares method on F^2 using SHELXL-2018 included in OLEX 2 version 1.3.0.[3] The packing diagrams were made using Mercury 4.2.0.[4]

All other non-hydrogen atoms of complexes **1** - **3** were refined anisotropically and hydrogen atoms were labeled to ideal positions and refined isotropically using a riding model. All the diffused electron density of highly disordered solvent molecules cannot be modelled properly. Therefore, SOLVENT MASK procedure in OLEX 2 has been used to mask the diffused electron density. SOLVENT MASK procedure details and corresponding results are provided in the respective CIF files. CCDC 2020246 – 2020248 and 2042421 contains the supplementary crystallographic data for this paper. These data can be obtained free of charge from The Cambridge Crystallographic Data Centre via www.ccdc.cam.ac.uk/data_request/cif.

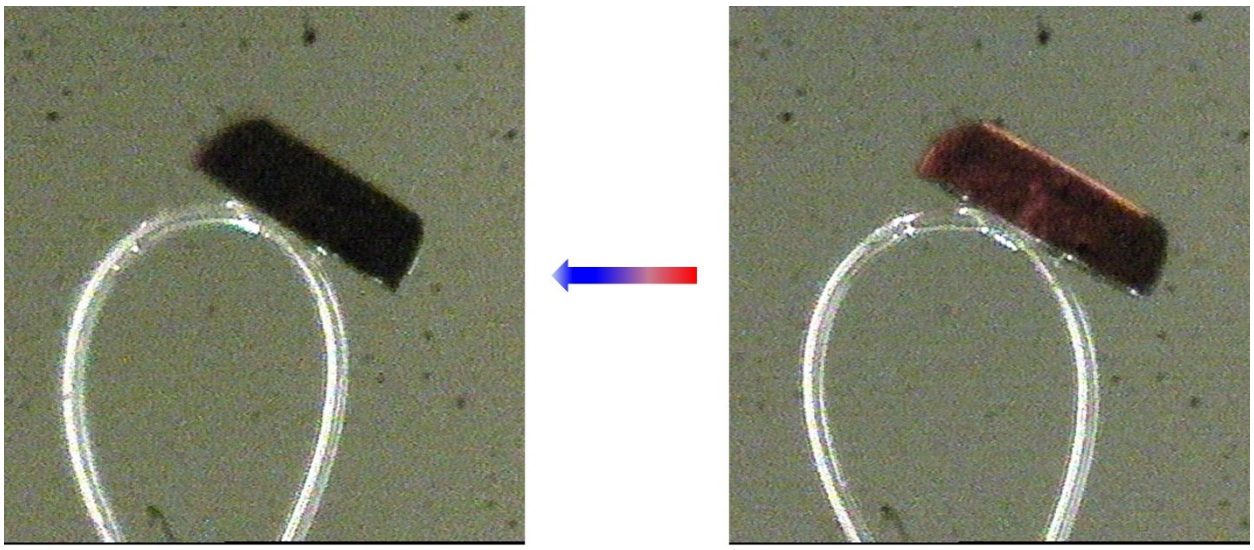

Scheme S1 Images of a single crystal of **3** at 200 K and 90 K showing a change in color from red to dark red.

Optical reflectivity measurements

The surface reflectivity measurements have been performed with a home-built system, operating between 10 and 270 K and in a spectrometric range from 400 – 1000 nm. For dark sample we have diluted the samples using $BaSO_4$ for better resolution. A halogen-tungsten light source (Leica CLS 150 XD tungsten halogen source adjustable power from 0.05 mW cm^{-2} to 1 W cm^{-2}) was used as the spectroscopic light. The measurements were calibrated by barium sulphate as a reference sample. With this reflectivity technique, the absolute reflectivity (*AR*) at a specific wavelength λ is plotted as $AR(\lambda = (R_{sample}(\lambda) - R_{dark}(\lambda)) / (R_{ref}(\lambda) - R_{dark}(\lambda))$. The corresponding spectra $AR(\lambda)$ can be viewed as a mirror image of the absorbance spectra: *i.e.*, when the sample absorbs efficiently (or weakly) the light, a low (or high, respectively) value of AR is measured. As the samples are potentially very photo-sensitive, the light exposure time was minimized during the experiments keeping the samples in the dark except during the spectra measurements when white light is shined on the sample surface (Power = 0.5 mW cm^{-2}). For all the excitation/de-excitation experiments performed at 10 K, the sample was initially placed at 270 K and then at the low temperature keeping the sample in the dark to avoid any excitation. Heating and cooling measurements were carried out at 4 K min^{-1}, whereas the relaxation experiment

was performed with a sweep rate of 0.4 K min^{-1}. For white light irradiation, the source described above was used, but continuously with a power of 0.5 mW cm^{-2} and the light is only switched on for 1 second to record the reflectivity spectrum at a given temperature, and then the light is switched off during the next temperature step.

The reflectivity properties of **3** were further investigated using specific wavelengths for photo-excitation experiments. Compared to the above optical measurements, the white light is still used as a light probe for spectroscopy, but the set-up of 14 different Light Emitting Diodes (LEDs from Thorlabs) operating between 365 and 1050 nm (at 365, 385, 405, 455, 505, 590, 625, 660, 735, 780, 850, 940 and 1050 nm) was used for the excitation experiments.

Detailed measurements were performed in order (i) to find the most efficient wavelength for irradiation, (ii) at this optimum wavelength, to study the effect of the light power under a fixed irradiation time. To test the different LEDs, the following protocol was applied: the compound was placed at 10 K in its diamagnetic state after cooling at 10 K/min in the dark, and a spectrum is first collected. Then the compound is irradiated with one LED for 20 minutes. A new spectrum is recorded. To recover the diamagnetic state, the compound is heated at 200 K and then placed again in the dark at 10 K at 10 K/min, before finally being irradiated with another LED. This procedure is repeated for each LED. The results for the different LEDs are shown below. The most important changes in the spectra before and after 20 minutes of irradiation are observed with the 590 nm LED in ON mode and 850 nm LED for OFF mode.

Photoluminescence Measurements

Edinburg Instruments FLS920 Fluorescence Spectrometer with a 450 W continuous Xe arc lamp as an excitation source was used for steady-state photoluminescence measurements. For variable temperature measurements, a sample in the form of a 6 mm diameter pellet was glued with silver paste on the Cu stage, in the cryo chamber. Optical fiber was used to impinge the photons on sample and to direct the emitted photons

towards the detector. Variation in the temperature was carried out in the closed cycle He-cryostat (Cryo Industries Ink.) with the help of Keithly 668 temperature controller.

Figures

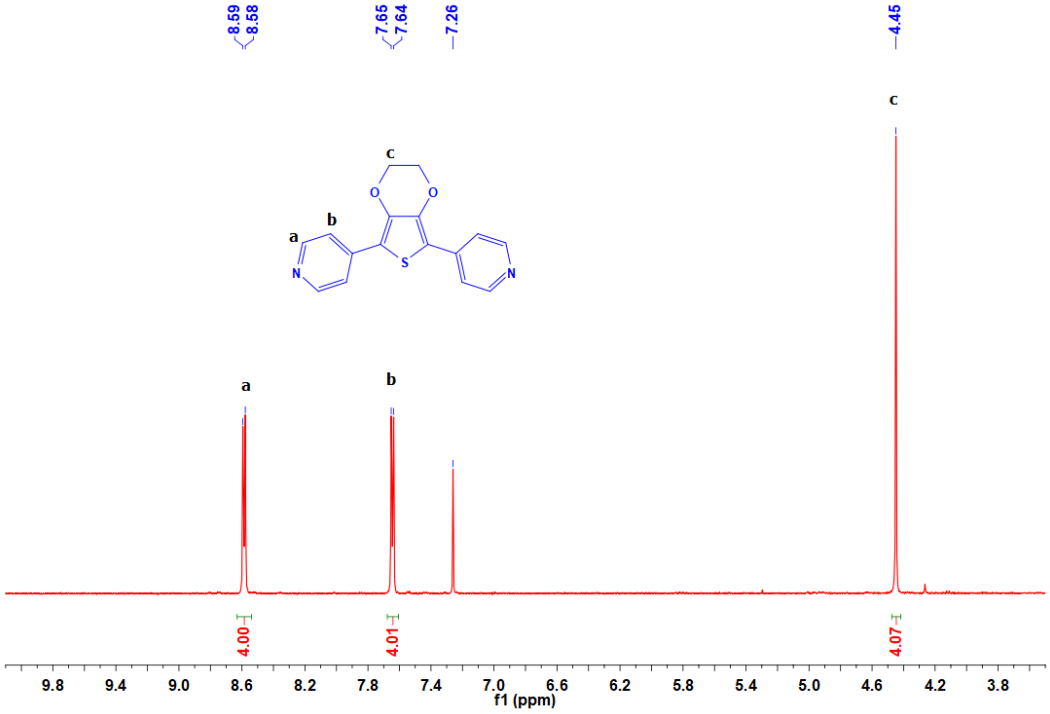

Fig. S1. ^{1}H NMR ($CDCl_3$, 500 MHz) spectrum of **L1**.

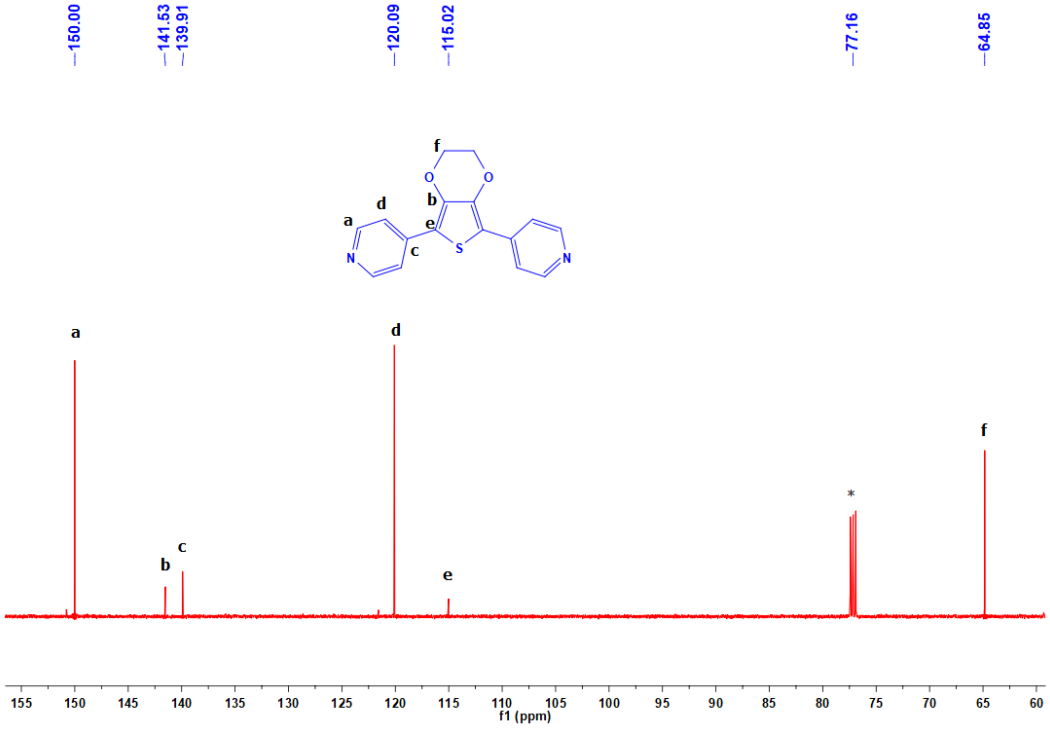

Fig. S2. ^{13}C NMR ($CDCl_3$, 125 MHz) spectrum of **L1**.

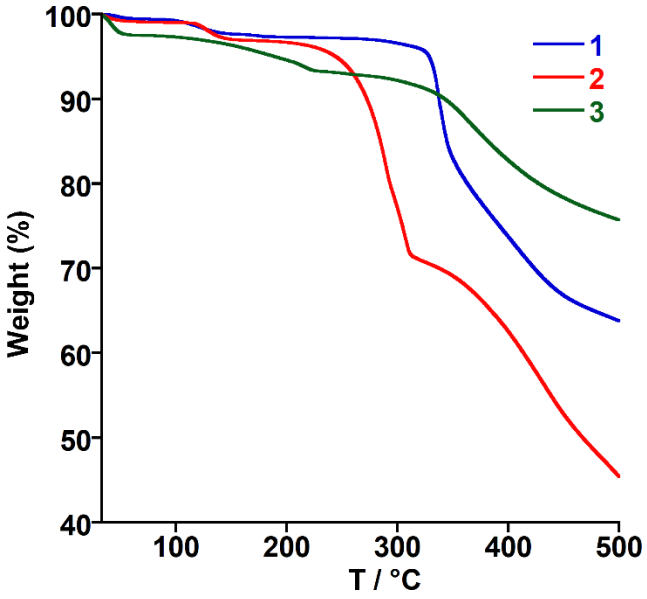

Fig. S3. Thermogravimetric analysis (TGA) curves for **1** - **3** from 30 to 600°C at a 10 °C min^{-1} temperature rate under N_2 atmosphere.

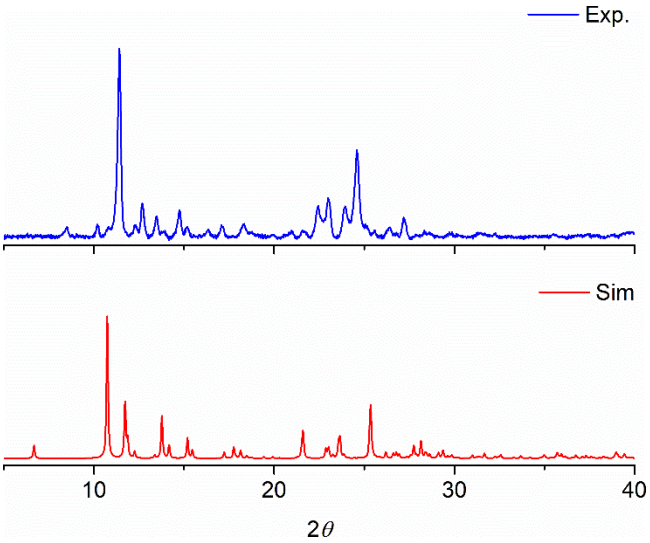

Fig. S4. Comparison of the room temperature experimental PXRD pattern and the 120 K simulated one for **1**.

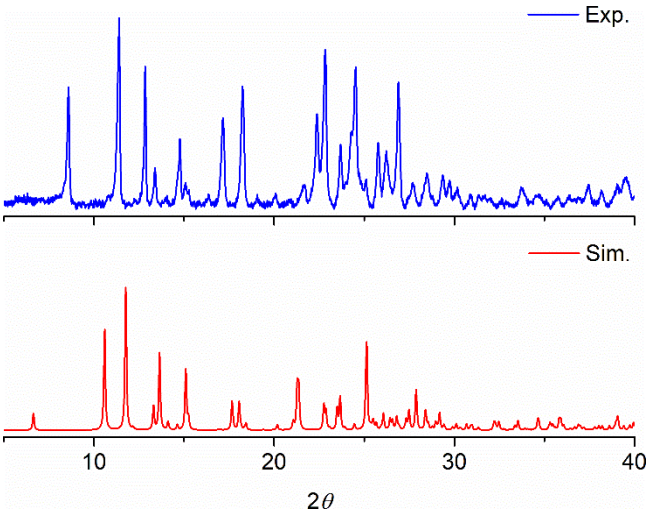

Fig. S5. Comparison of the room temperature experimental PXRD pattern and the 120 K simulated one for **2**.

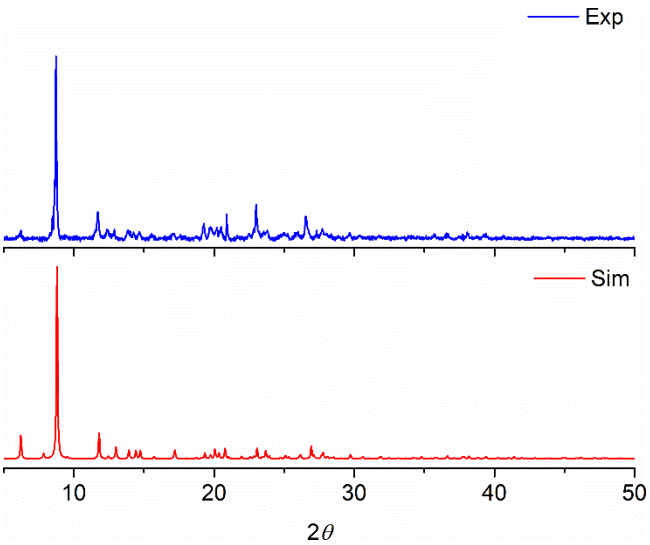

Fig. S6. Comparison of the room temperature experimental PXRD pattern and the 200 K simulated one for **3**.

Spectroscopy Studies

Complexes **1**-**3** were well characterized by solid-state infrared (IR) spectroscopy at room temperature (Fig. S7). IR spectroscopy is a powerful tool to characterize the spin-state of iron(II) center containing N-coordinated NCX^- (X = S, Se) coligands as the stretching vibration of N≡C bond has been significantly affected by the spin-state of the iron(II) center. It has been noticed that the HS iron(II) complex displays absorption between 2020 and 2060 cm^{-1} while absorption

at around 2100 cm^{-1} characterizes the LS state.[5] IR spectra of all three iron(II) complexes show strong sharp peaks at 2046, 2059 cm^{-1} for **1** and 2048, 2064 cm^{-1} for **2** with a shoulder at 2073 cm^{-1} for **1** and 2077 cm^{-1} for **2** which are the characteristic N≡C stretching frequency for coordinated NCS^- and $NCSe^-$ coligands respectively. These values are in good agreement with HS state of iron(II) in **1** and **2** at room temperature. In addition, both complexes display typical absorptions of coordinated **L1** ligand at around 1596, 1540, 1444, 1218, 1075 and 655 cm^{-1}. N≡C stretching frequency for coordinated NCS^- coligands of **3** was observed as a strong sharp peak at 2051 cm^{-1}. In addition, a sharp peak at 2194 cm^{-1} was detected, characteristic stretching frequency of C≡C bond of coordinated **L2** ligand, which is blue-shifted in comparison to free ligand (2200 cm^{-1}). Moreover, the spectrum exhibits characteristic absorptions of coordinated **L2** ligand at around 1571, 1446, 1416, 1264, 1076, 1009, 826, 750 and 544 cm^{-1}. All these values indicate the HS iron(II) state in **3** at room temperature.

Electronic absorption spectroscopy of both ligands and three complexes have also been studied in solution and solid-state (Fig. S8-S10). UV-Vis spectra of the complexes (**1** and **2**) in methanol show band at 429 and 439 nm respectively, which attribute to the ligand to metal charge transfer (LMCT) transitions. Further, the spectra display ligand-based (**L1**) charge transfer bands at around 265, 330 and 363 nm corresponding to the ligand spectrum. As shown in Fig. S10, solid-state UV-Vis-NIR spectra of complexes **1** and **2** show similar LMCT and ligand-based charge transfer absorptions with d-d transition bands at around 850 nm and 1150 nm. The comparison with the solution spectra suggested that complexes **1** and **2** preserved their identity upon dissolution. The solid-state UV-Vis-NIR spectrum of complex **3** shows a shoulder at around 555 nm which can be ascribed to the LMCT transitions. In addition, the spectrum exhibit d-d transition band at about 1000 nm with **L2** ligand-based charge transfer transition band at around 395 nm. These values indicate HS iron(II) in all three complexes at room temperature.

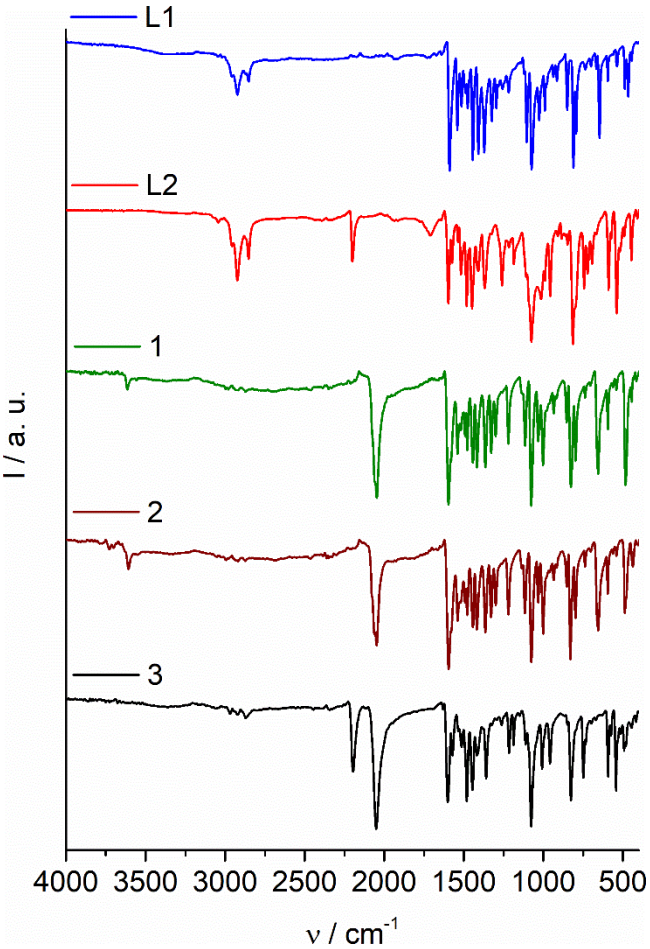

Fig. S7. IR spectra of ligands **L1** and **L2** with complexes **1** - **3** at RT.

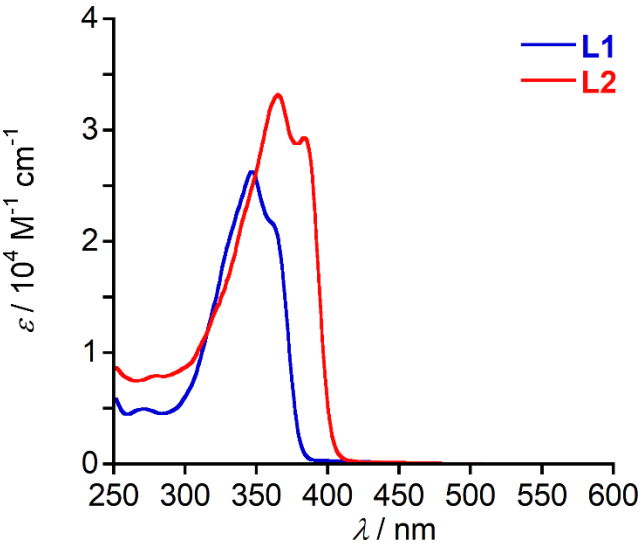

Fig. S8. UV-vis spectra of **L1** and **L2** in DCM at room temperature.

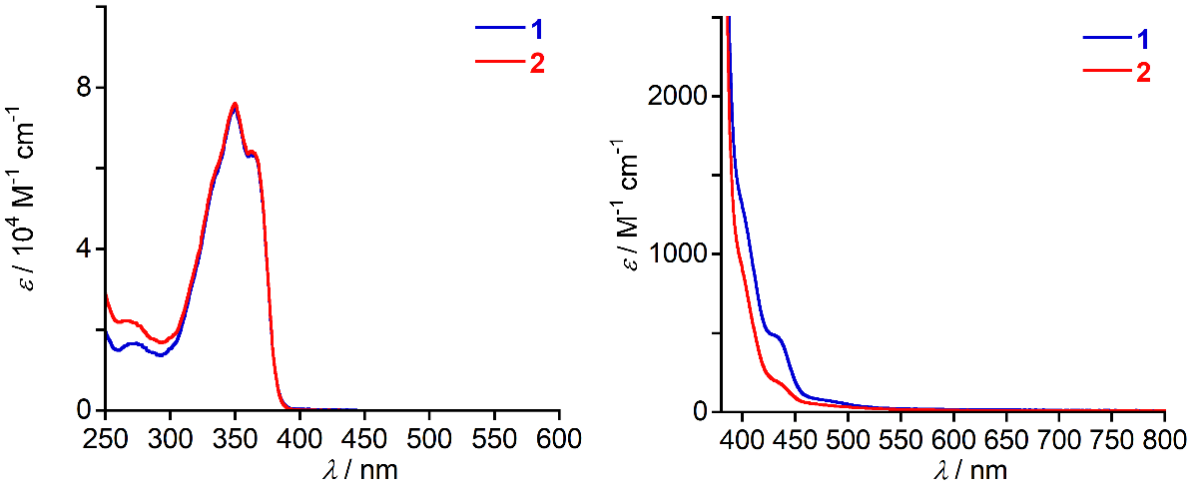

Fig. S9. UV-vis-NIR spectra of **1** and **2** in MeOH with dilute (left) and concentrated (right) solutions at room temperature.

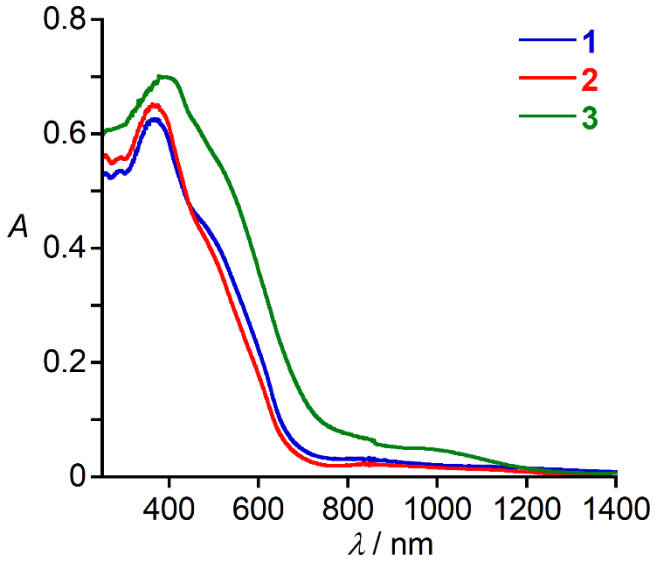

Fig. S10. Solid state UV-vis-NIR spectra of **1** - **3** at room temperature.

Electrochemical Studies

Electrochemical investigations suggest that ligand **L1** shows irreversible oxidation at E_{pc} = 0.52 *vs* *Fc/Fc*$^+$ in DCM (Fig. S11).[6] Cyclic voltammogram and square wave voltammogram of complex **1** reveal two irreversible oxidations around E_{pc} = 0.08 V and 0.42 V *vs* *Fc/Fc*$^+$ (Fig. S12 and S13) corresponding to the oxidation of ligand coordinated to iron(II) center and metal coordinated **L1** ligand respectively. For complex **2**, ligand coordinated iron(II) center-based irreversible oxidation has been observed at around 0.08 V *vs* *Fc/Fc*$^+$ (Fig. S14 and S15). In addition, voltammograms of

1 and **2** also display a coordinated ligand based irreversible reduction at around E_{pa} = -1.31 V *vs Fc/Fc*$^{+}$. Similar to 2D CN [Fe(**L2**)$_2$(NCSe)$_2$]$_n$,[1] two irreversible oxidations at around E_{pc} = 0.10 V and 0.65 V *vs Fc/Fc*$^{+}$ with a coordinated ligand-based irreversible reduction process at around E_{pa} = -0.79 V *vs Fc/Fc*$^{+}$ (Fig. S16 and S17) were observed for the *in-situ* reaction mixture of Fe:2NCS and **L2** in MeOH/DCM at room temperature.

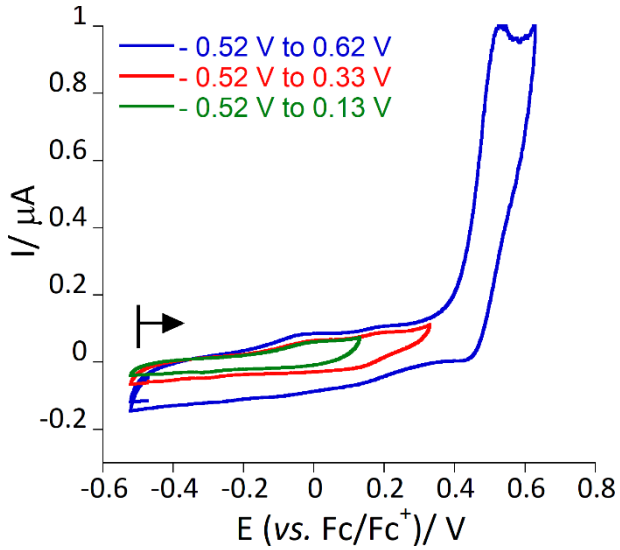

Fig. S11. Cyclic voltammograms of the ligand **L1** in DCM containing 0.1 M (^{n}Bu$_4$N)PF$_6$ at room temperature with a scan rate of 0.1 V/s. Arrows indicate the open circuit potential with the direction of the potential sweep .

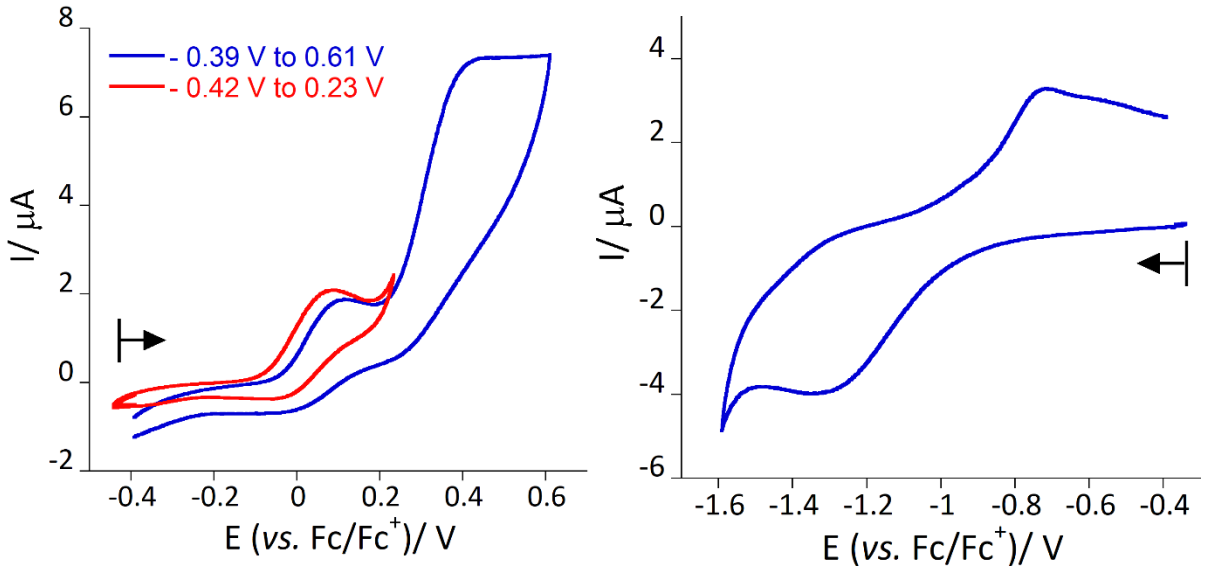

Fig. S12. Cyclic voltammograms for the oxidation (left) and reduction (right) of **1** in MeOH/DCM containing 0.1 M (^{n}Bu$_4$N)PF$_6$ with a scan rate of 0.1 V/s at room temperature. Arrows indicate the open circuit potential with the direction of the potential sweep.

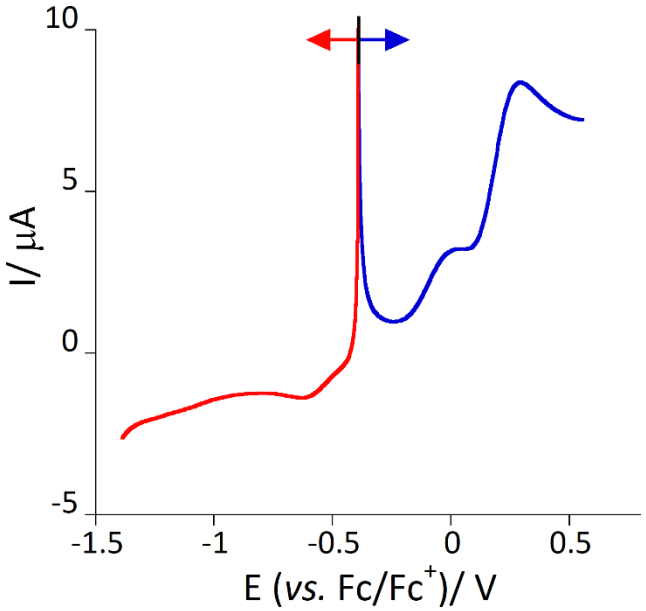

Fig. S13. Square wave voltammograms of **1** in MeOH/DCM containing 0.1 M (^{n}Bu$_4$N)PF$_6$ at room temperature. Arrows indicate the open circuit potential with the direction of the potential sweep.

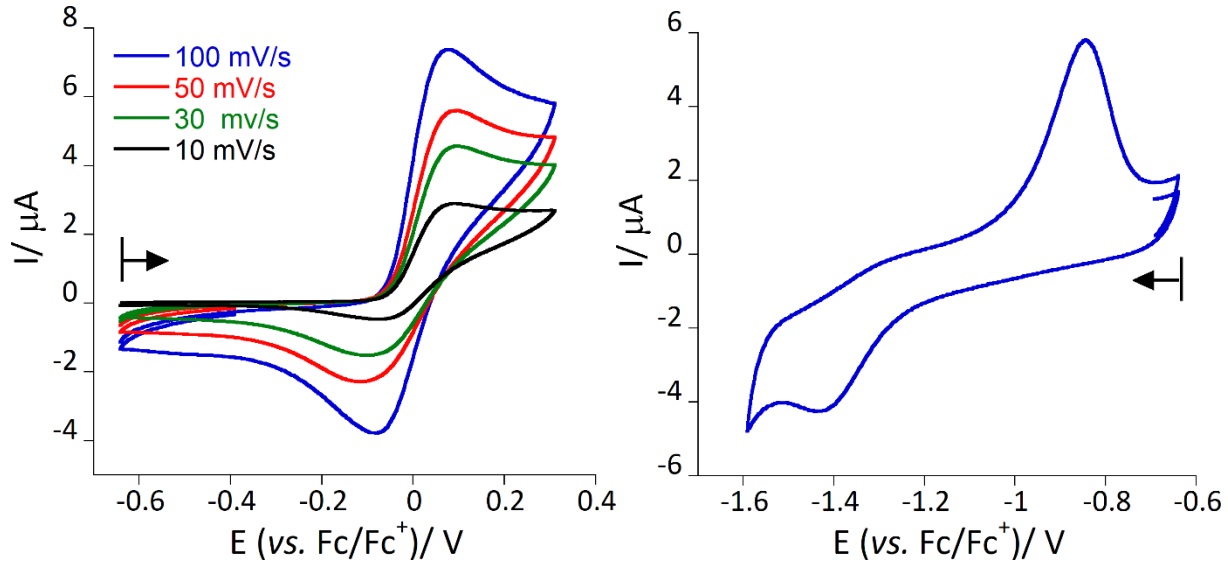

Fig. S14. Cyclic voltammograms for the oxidation (left) with various scan rates and reduction (right) of **2** in MeOH/DCM containing 0.1 M (^{n}Bu$_4$N)PF$_6$ with a scan rate of 0.1 V/s at room temperature. Arrows indicate the open circuit potential with the direction of the potential sweep.

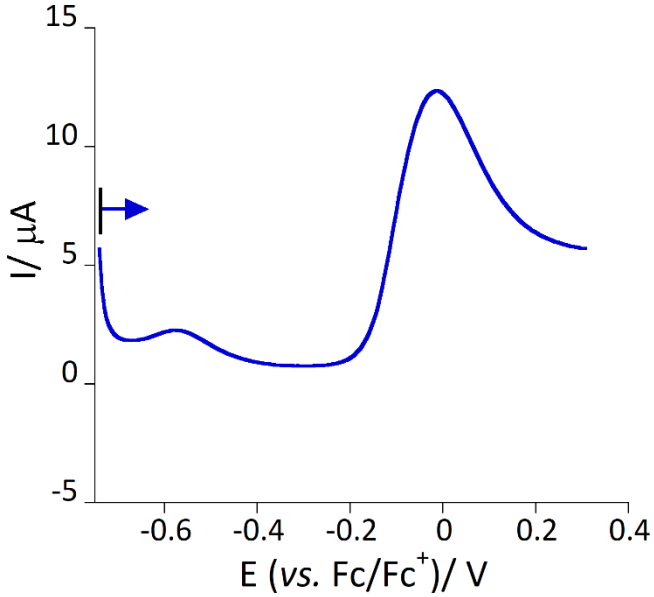

Fig. S15. Square wave voltammograms of **2** in MeOH/DCM containing 0.1 M (^{n}Bu$_4$N)PF$_6$ at room temperature. Arrows indicate the open circuit potential with the direction of the potential sweep.

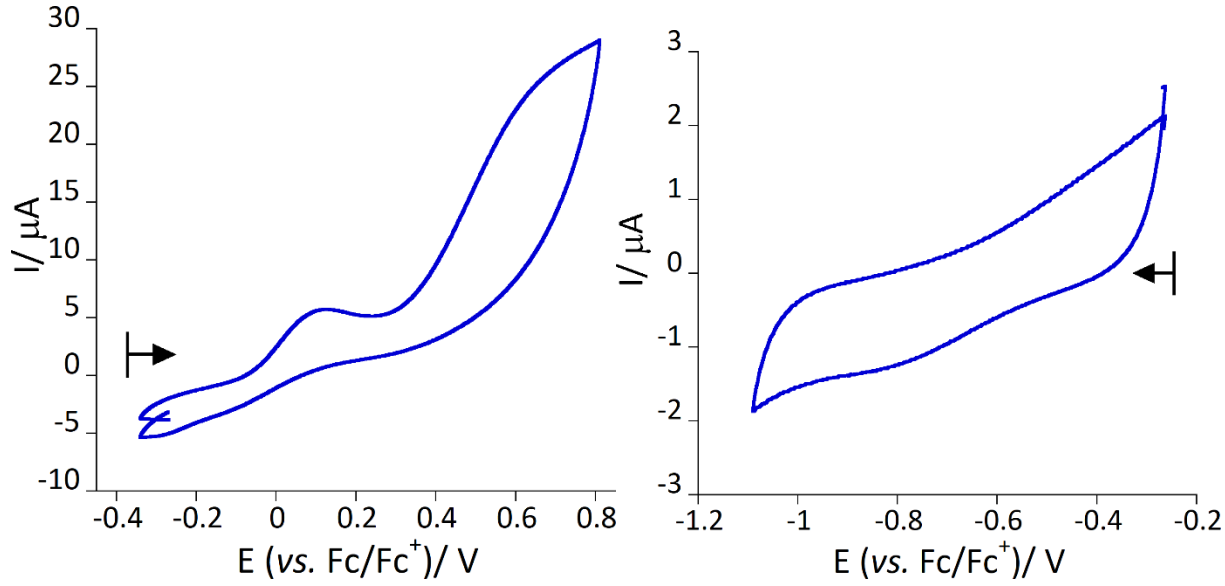

Fig. S16. Cyclic voltammograms of the reaction mixture of $Fe(NCS)_2$ and two equivalents of **L2** in DCM/MeOH (1:1) containing 0.1 M (^{n}Bu$_4$N)PF$_6$ at room temperature with a scan rate of 0.1 V/s, oxidation (left) and reduction (right). Arrows indicate the open circuit potential with the direction of the potential sweep.

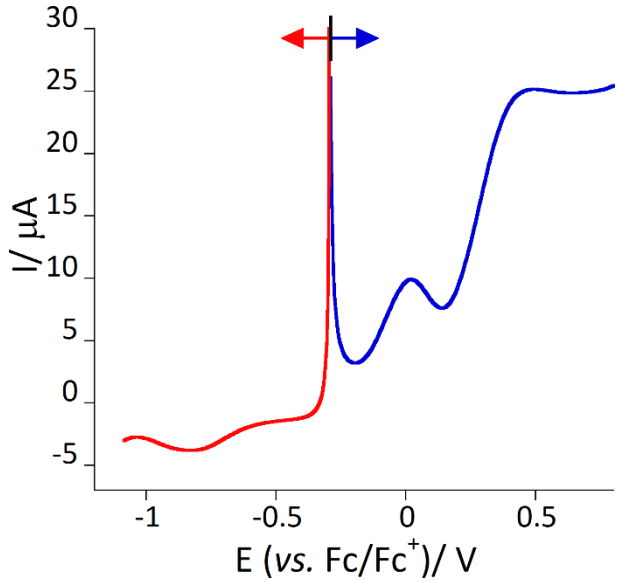

Fig. S17. Square wave voltammograms of the reaction mixture of $Fe(NCS)_2$ and two equivalents of **L2** in DCM/MeOH (1:1) containing 0.1 M (^{n}Bu$_4$N)PF$_6$ at room temperature. Arrows indicate the open circuit potential with the direction of the potential sweep.

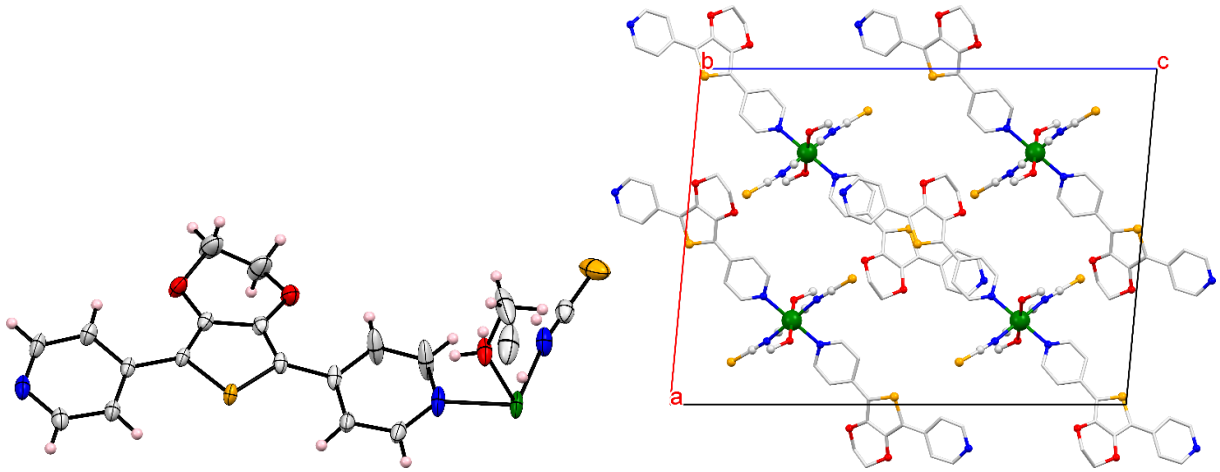

Fig. S18. Left: ORTEP view of asymmetric unit in **1**. Right: Unit cell diagram showing along *b*-axis in **1** at 120 K. Hydrogen atoms are omitted for clarity (Fe: green, C: gray, N: blue, O: red, S: orange, H: pink).

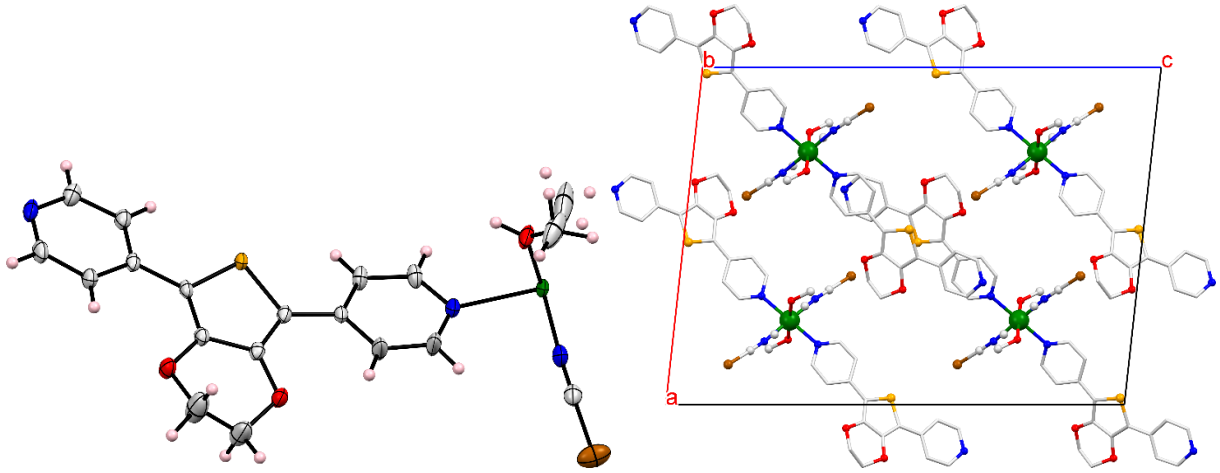

Fig. S19. Left: ORTEP view of asymmetric unit in **2**. Right: Unit cell diagram showing along *b*-axis in **2** at 120 K. Hydrogen atoms are omitted for clarity (Fe: green, C: gray, N: blue, O: red, S: orange, Se: brown, H: pink).

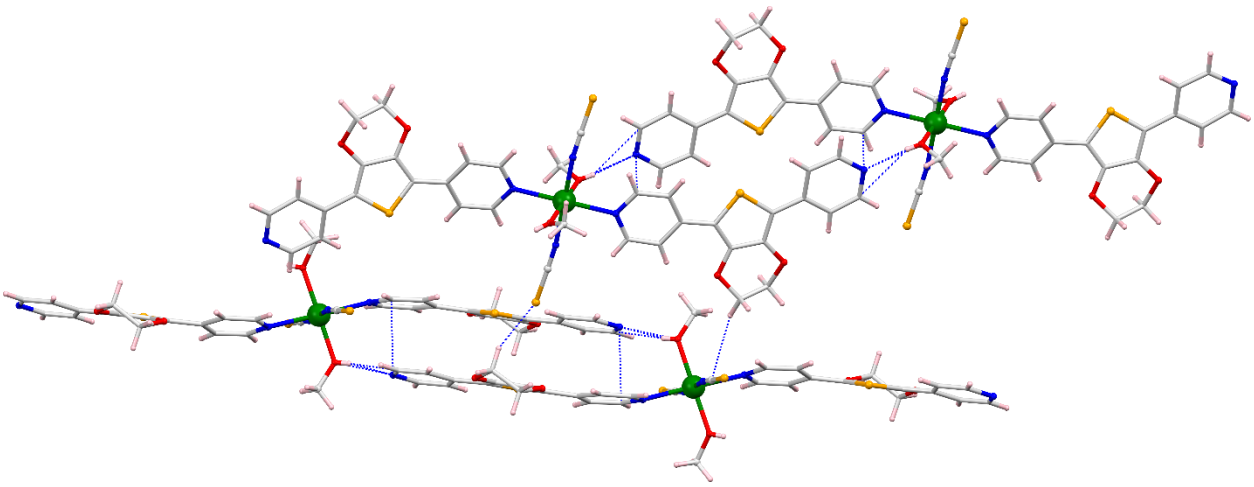

Fig. S20. A view of several weak supramolecular interactions presents between to lateral 1D chains in **1**. (Fe: green, C: gray, N: blue, O: red, S: orange; H: light pink).

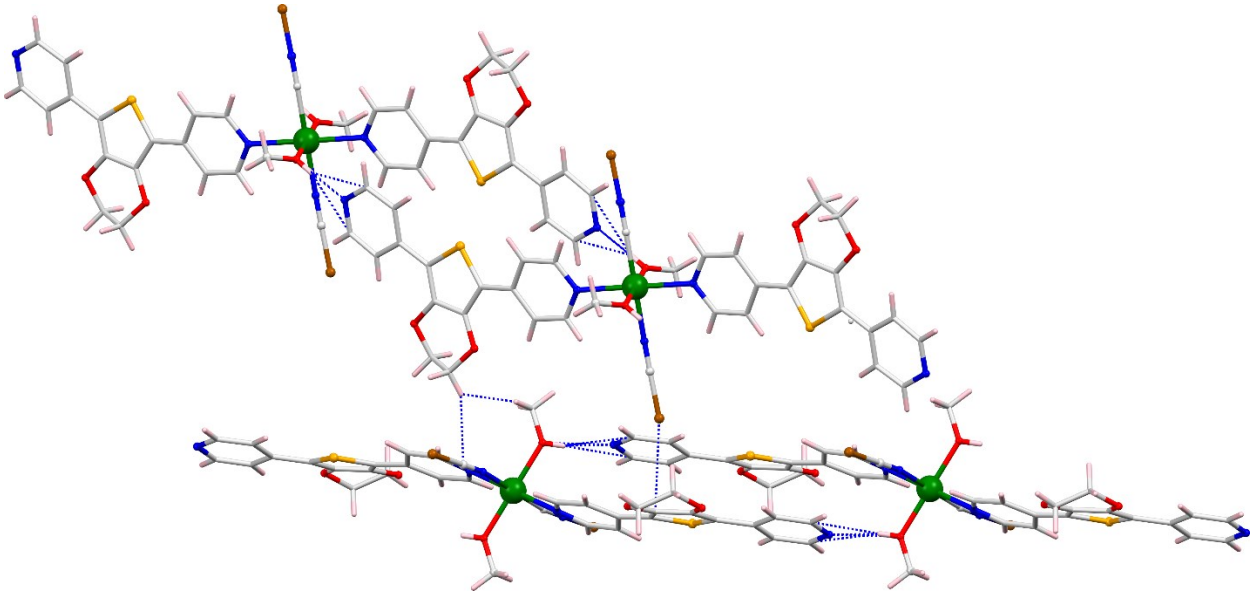

Fig. S21. A view of several weak supramolecular interactions presents between to lateral 1D chains in **2**. (Fe: green, C: gray, N: blue, O: red, S: orange; Se: brown; H: light pink).

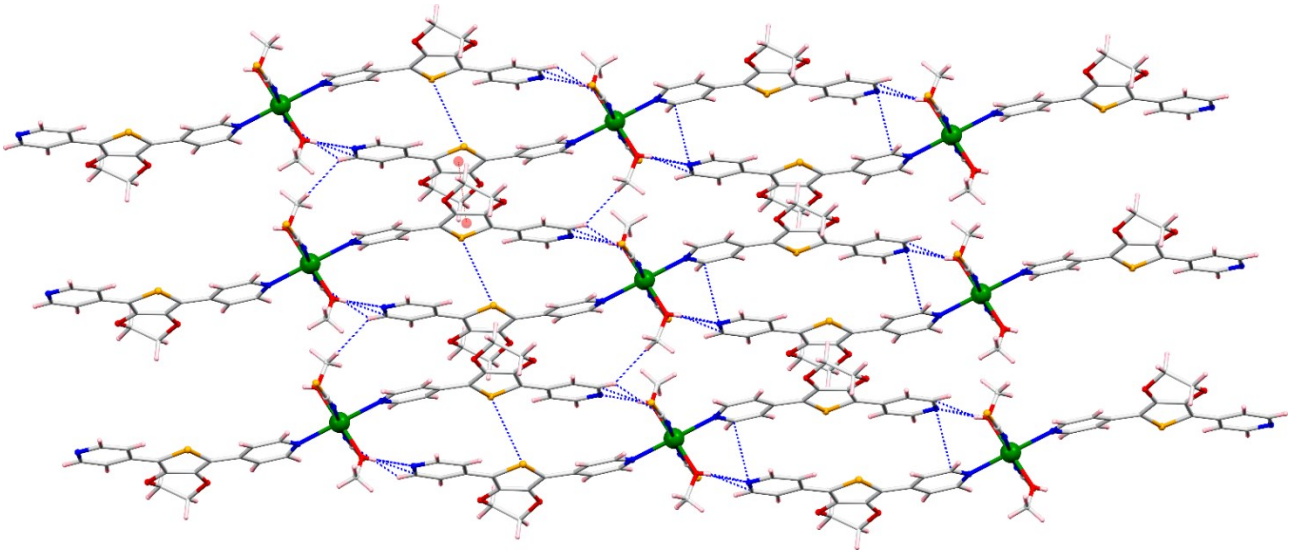

Figure S22. A view of 1D layer formed by several weak supramolecular interactions in **1** (Fe: green, C: gray, N: blue, O: red, S: orange; H: light pink).

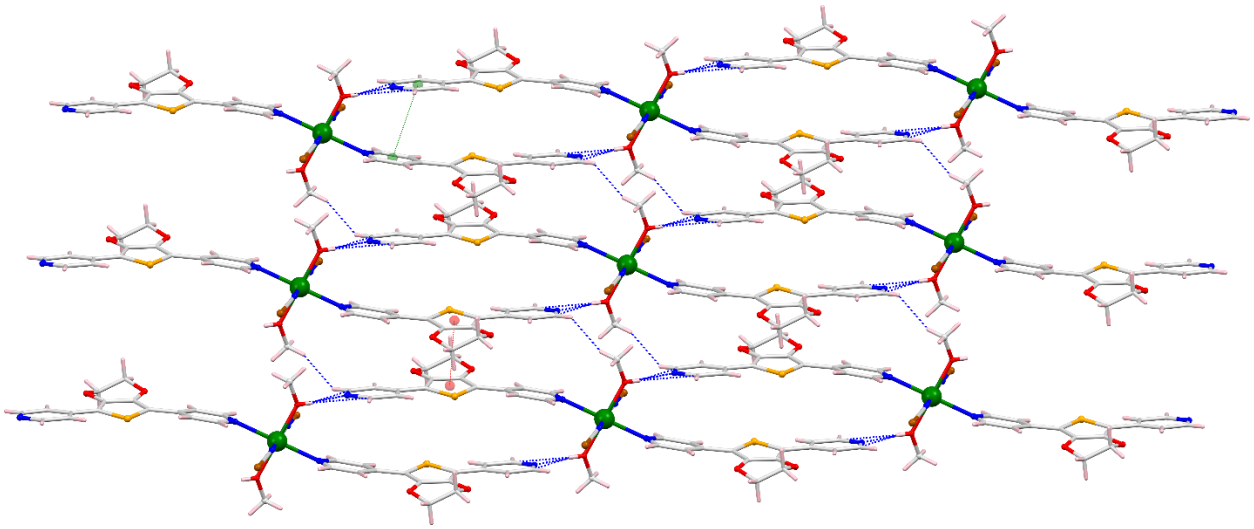

Fig. S23. A view of 1D layer formed by several weak supramolecular interactions in **2**. (Fe: green, C: gray, N: blue, O: red, S: orange; Se: brown; H: light pink)

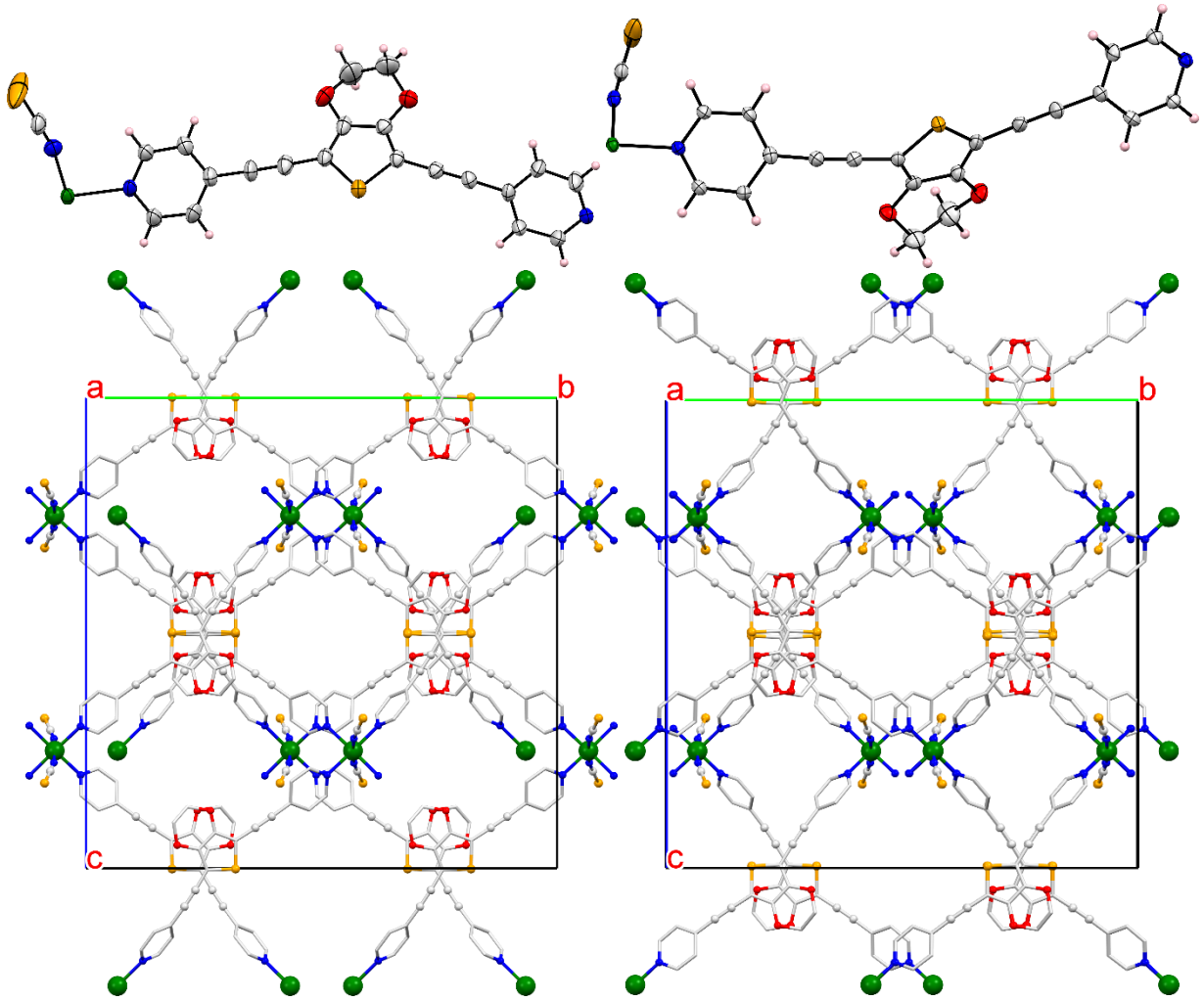

Fig. S24. Top: ORTEP view of asymmetric unit in **3** at 200 K (left) and 90 K (right). Bottom: Unit cell diagram showing void channels in **3** at 200 K (left) and 90 K (right). Hydrogen atoms are omitted for clarity (Fe: green, C: gray, N: blue, O: red, S: orange, H: pink).

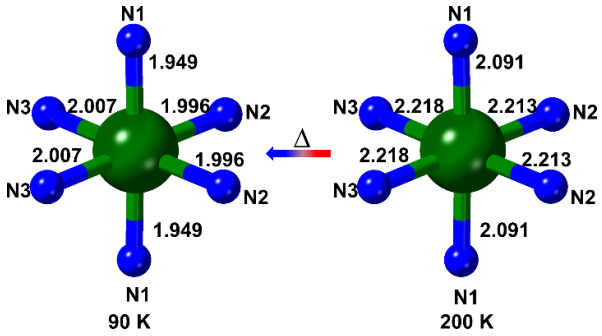

Fig. S25. Comparison of Fe–N distances in 3 at 200 and 90 K.

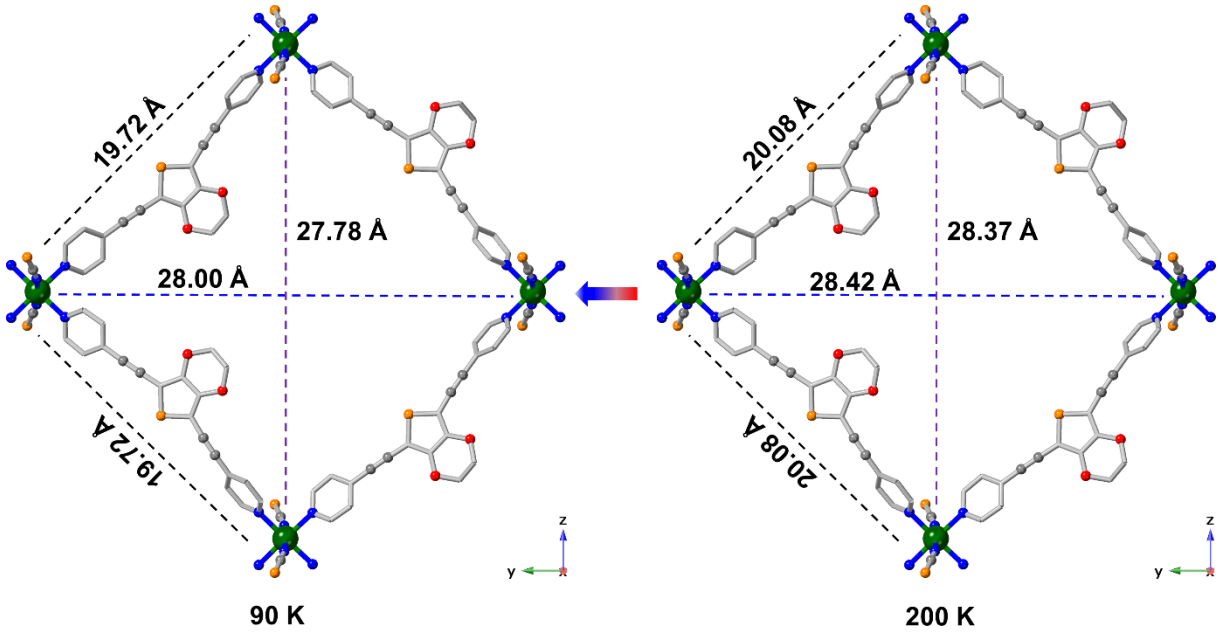

Fig. S26. Representation of the grid dimensional changes for **3** associated with the temperature change.

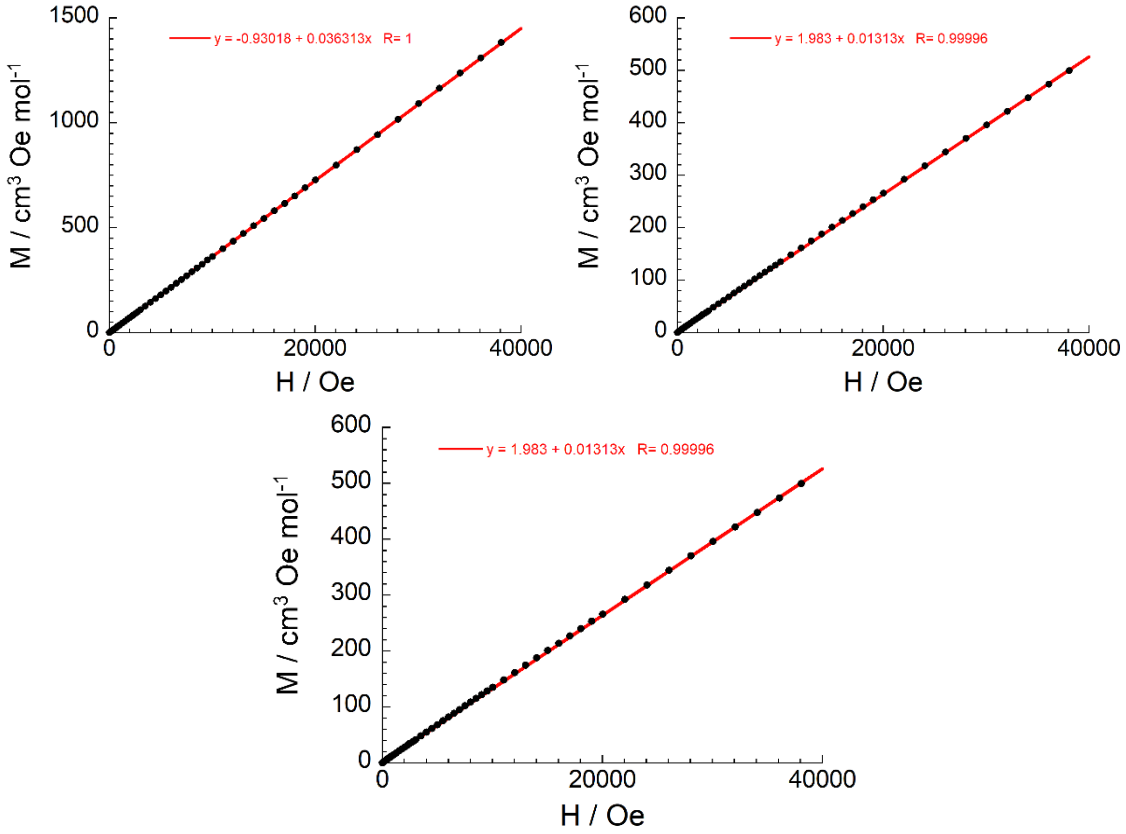

Fig. S27. Field dependence of the magnetization as *M* vs *H* plots for **1** (top, left), **2** (top, right) and **3** (bottom) at 100 K. The red line represents the best fit.

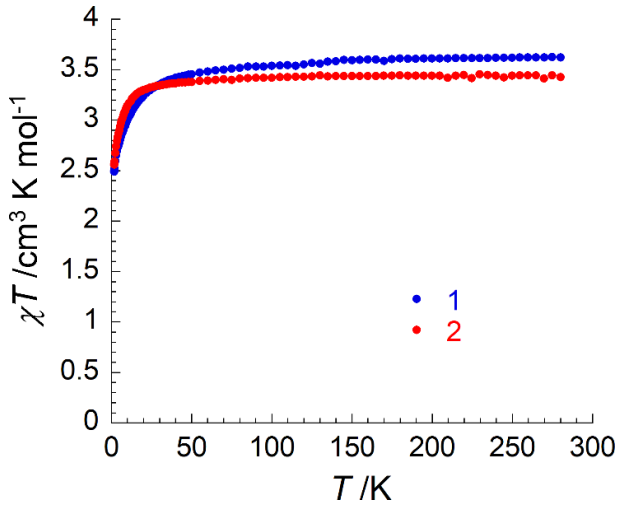

Fig. S28. Temperature dependence of χT product for **1** and **2** at 1000 Oe.

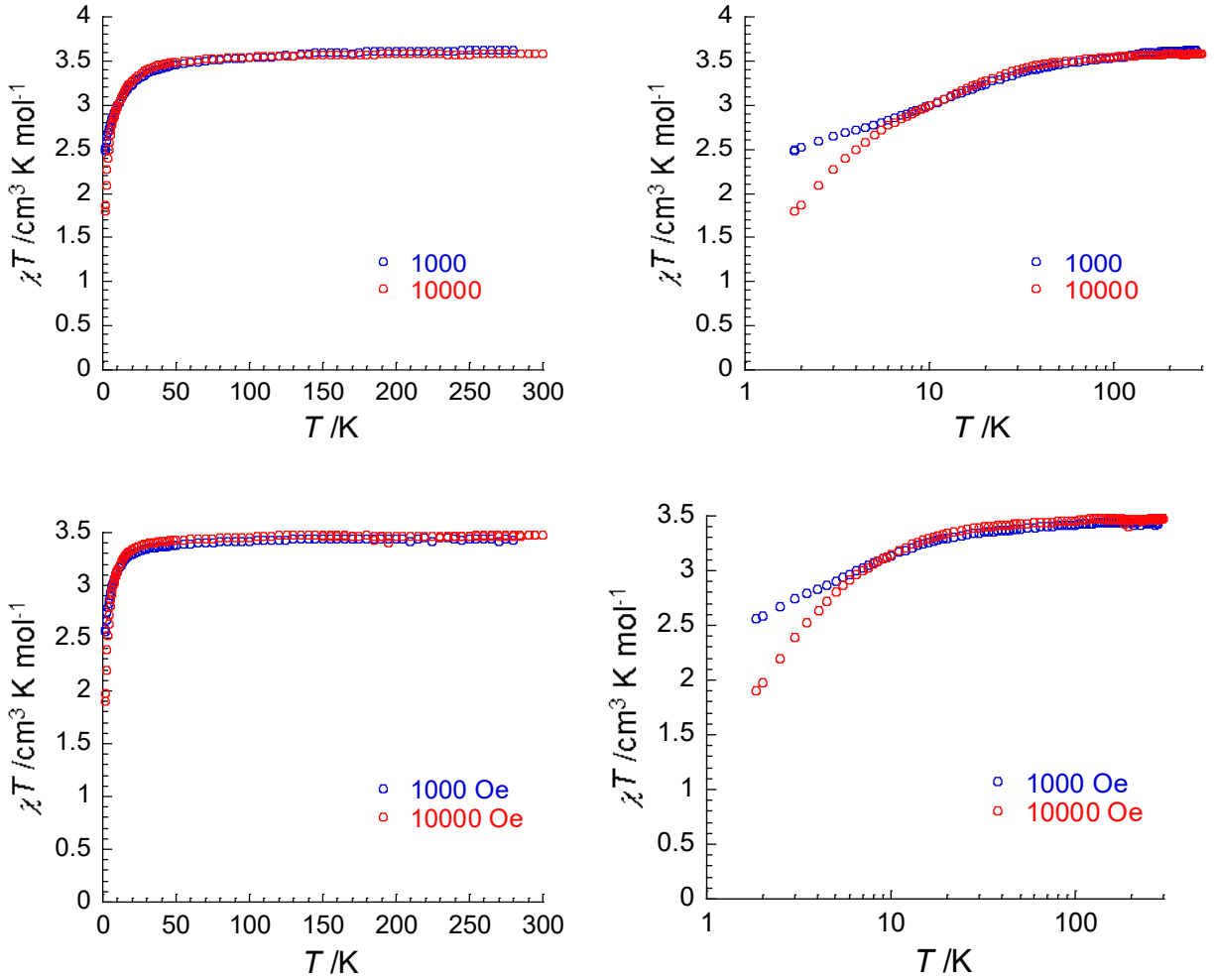

Fig. S29. Temperature dependence of the χT product of complexes **1** (top) and **2** (bottom) measured at H = 1000 and 10000 Oe plotted in normal scale (left) and log scale (right).

The field dependence of magnetization studies for **1** and **2** were carried out from 0 – 7 T at 1.85, 3, 5, and 8 K (Fig. S30 and S31). At 1.85 K, the magnetization values are observed around 2.80 and 3.3 μ_B for **1** and **2** respectively at 7 T, which are slightly lower than the expected value for one *S* = 2 system. In addition, *M vs H/T* measurements display non-superposition of the data on a single master curve, suggesting the presence of the magnetic anisotropy and/or low-lying excited states in these systems. No magnetic hysteresis was observed in *M vs H* at 1.85 K from -70000 Oe to + 70000 Oe with a sweep rate of 100 – 600 Oe. In order to understand the slow dynamics of magnetization, ac susceptibility measurements were carried out on **1** and **2** (Fig. S32 and S33). No out of phase (χ') signal was detected under zero dc field for both complexes **1** and **2**, indicating that effective quantum tunneling of magnetization (QTM) occurred at zero dc field. It is known and widely reported that the external magnetic field strongly affects the QTM. So, in order to minimize the probability of the quantum relaxation pathway in zero dc-field, the ac susceptibility was measured under different dc-fields. It is worth mentioning that no slow relaxation of magnetization was detected from the ac susceptibility measurements at 2 K in both complexes **1** and **2** even by using 1 T external magnetic field at driving frequencies 10 - 1000 Hz.

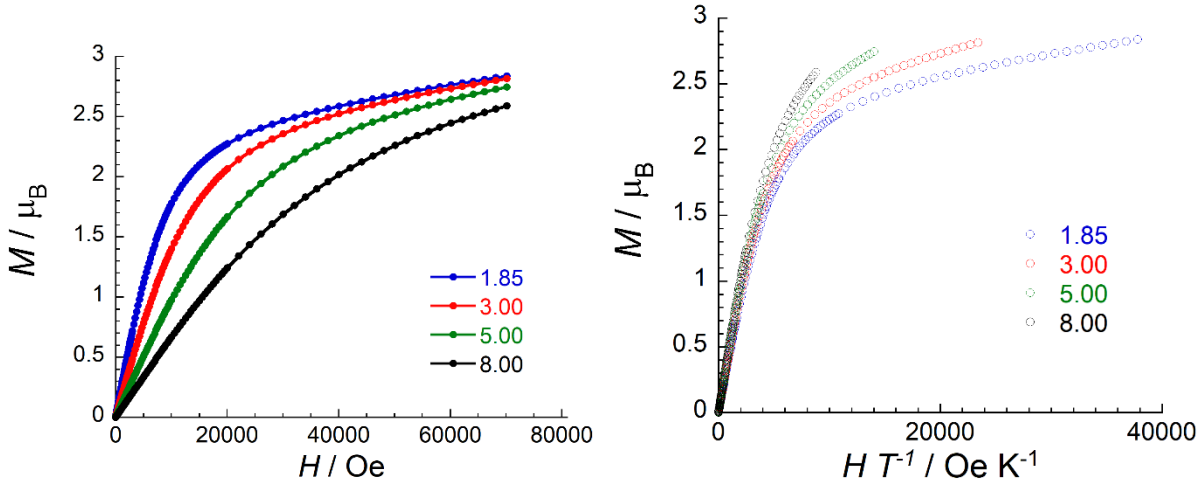

Fig. S30. Field dependence of the magnetization as *M* vs *H* (left) and *M* vs *H/T* (right) plots for **1** at 1.85, 3, 5 and 8 K. The solid lines are guide for the eyes.

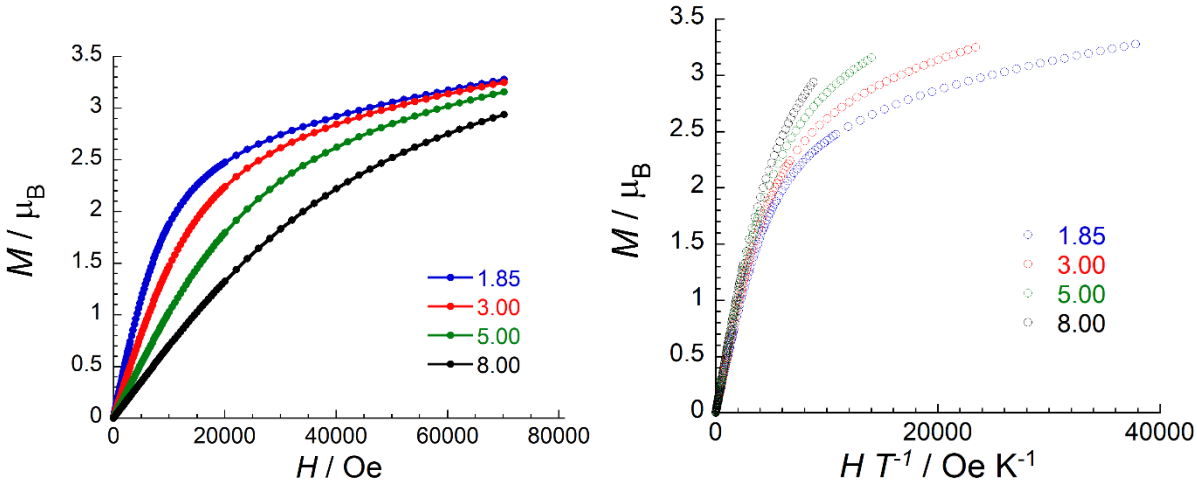

Fig. S31. Field dependence of the magnetization as *M* vs *H* (left) and *M* vs *H/T* (right) plots for **2** at 1.85, 3, 5, and 8 K. The solid lines are guide for the eyes.

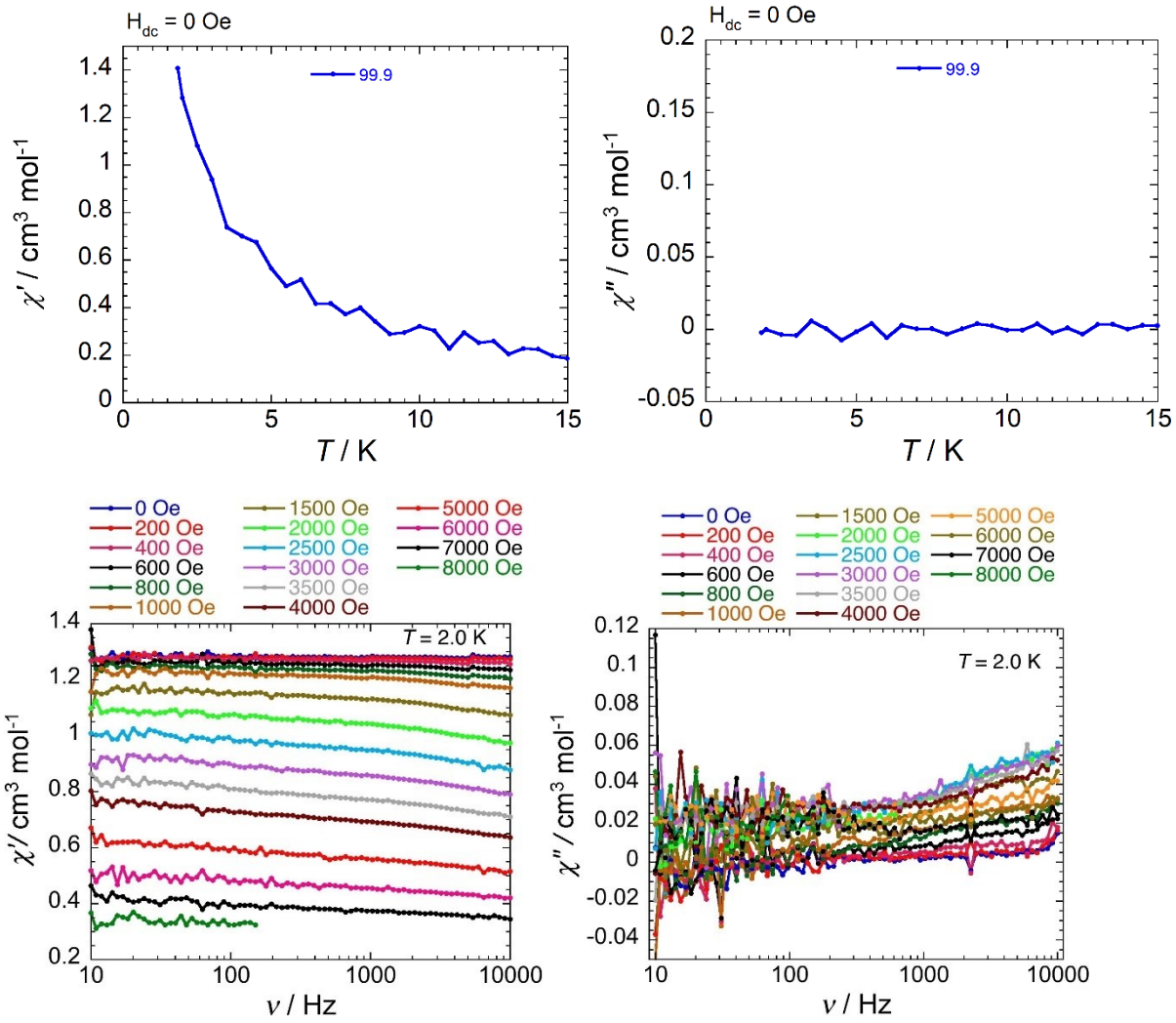

Fig. S32. Frequency vs temperature plot of the real (χ', left) and imaginary (χ'', right) components of the ac susceptibility at 0 Oe external dc field and different temperatures from 1.8 – 15 K (top) and different external dc field at 2 K (bottom), respectively with a 3 Oe ac field for a polycrystalline sample of **1**.

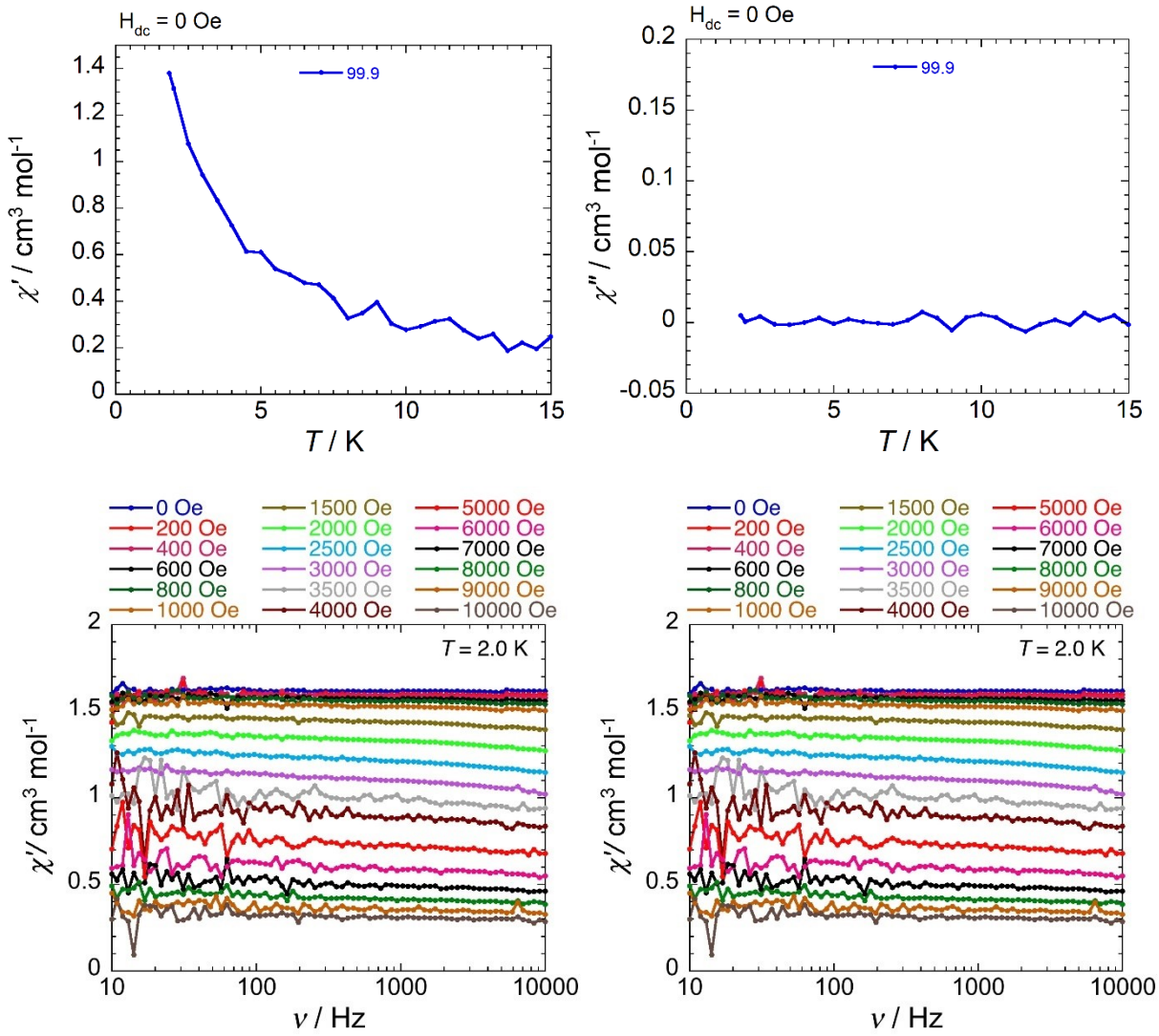

Fig. S33. Frequency vs temperature plot of the real (χ', left) and imaginary (χ'', right) components of the ac susceptibility at 0 Oe external dc field and different temperatures from 1.8 – 15 K (top) and different external dc field at 2 K (bottom), respectively with a 3 Oe ac field for a polycrystalline sample of **2**.

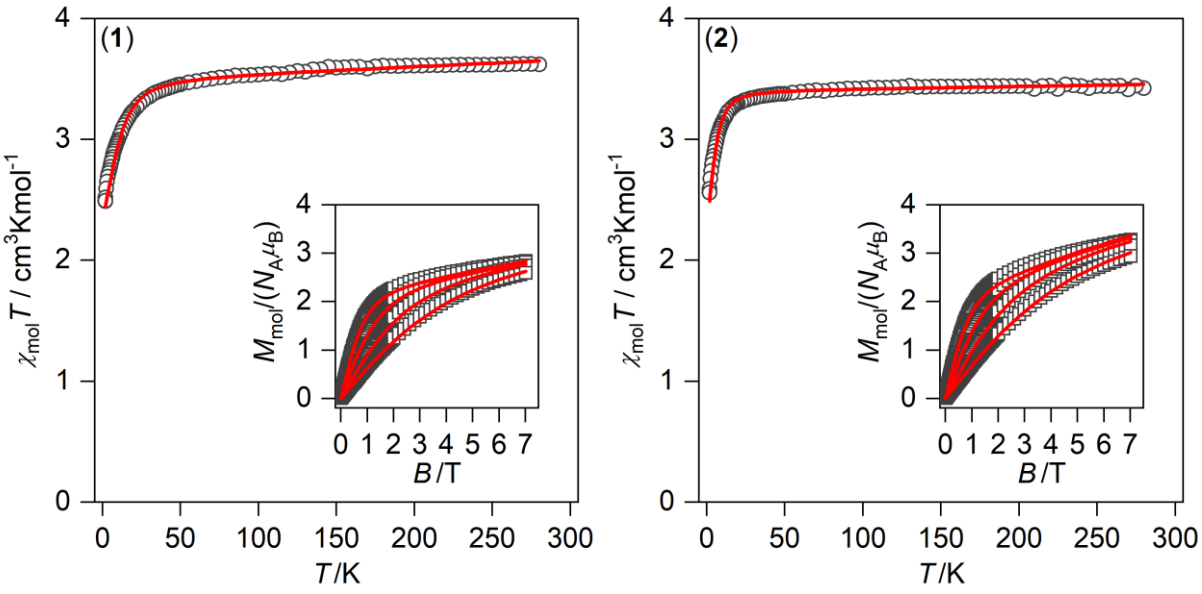

Fig. S34. Magnetic data for **1 - 2** showed as the temperature dependence of the χT product and the isothermal molar magnetization measured at T = 1.8, 3, 5, and 8 K in the inset. The empty symbols represent the experimental data; red full lines represent the fitted data using eqn (1) with spin Hamiltonian parameters listed in Table 2.

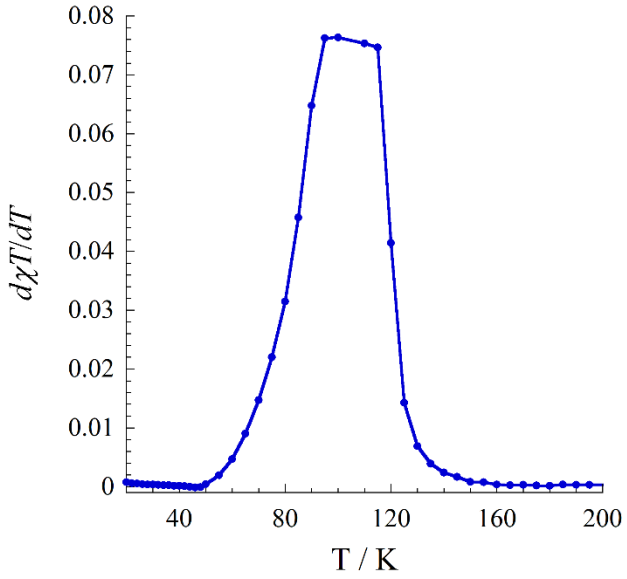

Fig. S35. The first derivative of χT against the temperature, dχT /dT *vs*. T, identifies $T_{1/2}$ = around 100 K for **3**.

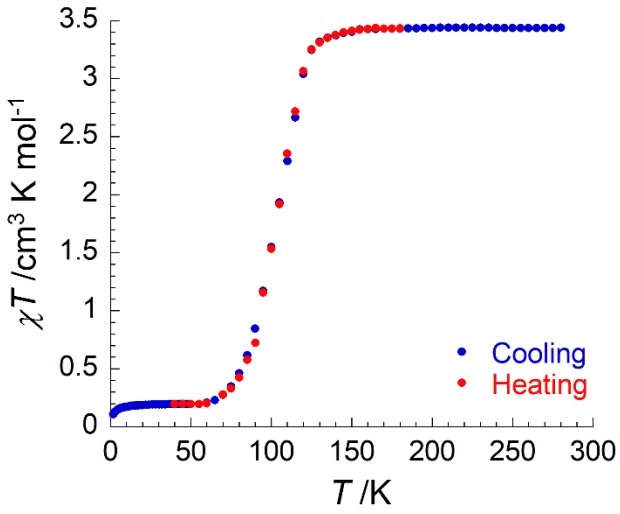

Fig. S36. Temperature dependence of the χT product of complex **3** in heating and cooling modes at 1000 Oe.

The following equation deduced from the ideal solution model was applied to fit the spin crossover properties observed by magnetic studies.

$$X = X_{LS} + \frac{X_{HS} - X_{LS}}{1 + \exp\left[\Delta H/R\,(1/T - 1/T_{1/2})\right]}$$

X = χT product

X_{LS} = χT product for pure low-spin

X_{HS} = χT product for pure high-spin

ΔH = Enthalpy change associated with the spin crossover phenomenon

R = Ideal gas constant

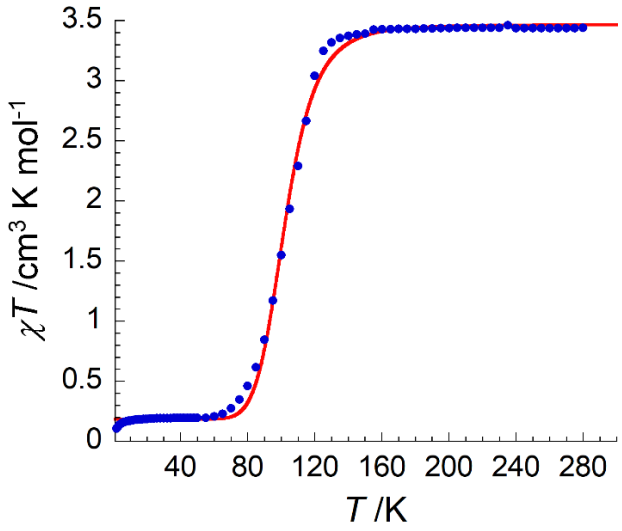

Fig. S37. χT *vs.* T data of complex **3** fit using the ideal solution model.

The ΔS value of 93 J K^{-1} mol^{-1} is larger than the calculated ΔS value considering only the electronic contribution (ΔS_e = Rln[(2L_{HS} + 1)(2S_{HS} + 1)/(2L_{LS} + 1)(2S_{LS} + 1)] = 22.5 J K^{-1} mol^{-1} for ^5T HS and ^1A LS spectroscopic terms in a perfect octahedron geometry which suggests a significant contribution of the intra- and inter-molecular vibrations in the entropy change during the spin-crossover process.

The field dependence of magnetization studies for **3** was carried out at 1.85, 3, 5, and 8 K (Fig. S38) from 0 – 7 T magnetic field. At 1.85 K, the magnetization value was observed at 0.17 μ_B at 7 T, which also confirms the presence of small residual HS iron(II) in the system. In addition, *M vs H/T* measurement displays non-superposition of the data on a single master curve, confirm the presence of the magnetic anisotropy and/or low lying excited states coming from the residual HS iron(II) ion. No out of phase (χ') signal was detected under zero dc field in this complex (Fig. S39).

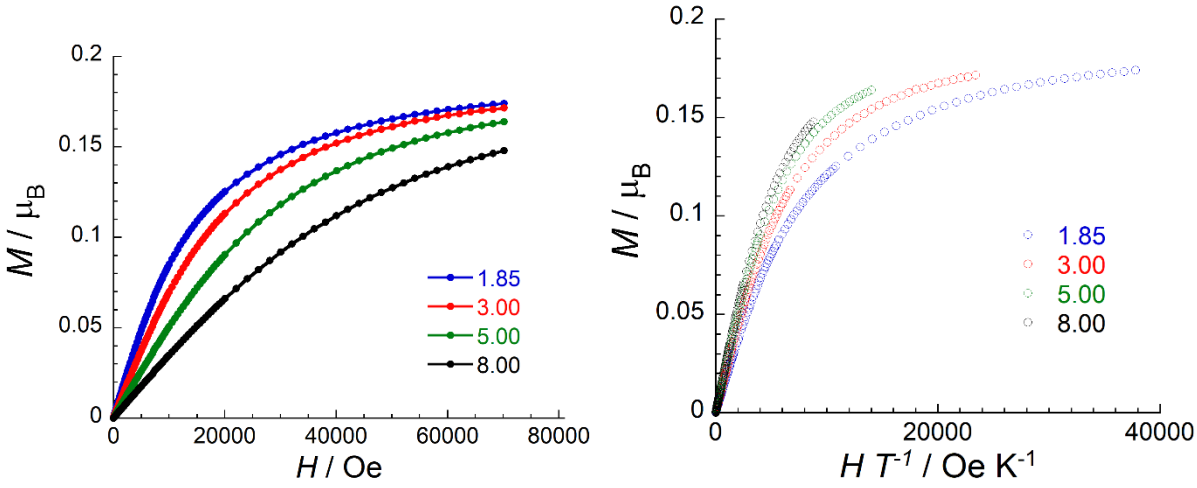

Fig. S38. Field dependence of the magnetization as *M* vs *H* (left) and *M* vs *H/T* (right) plots for **3** at 1.85, 3, 5 and 8 K. The solid lines are guide for the eyes.

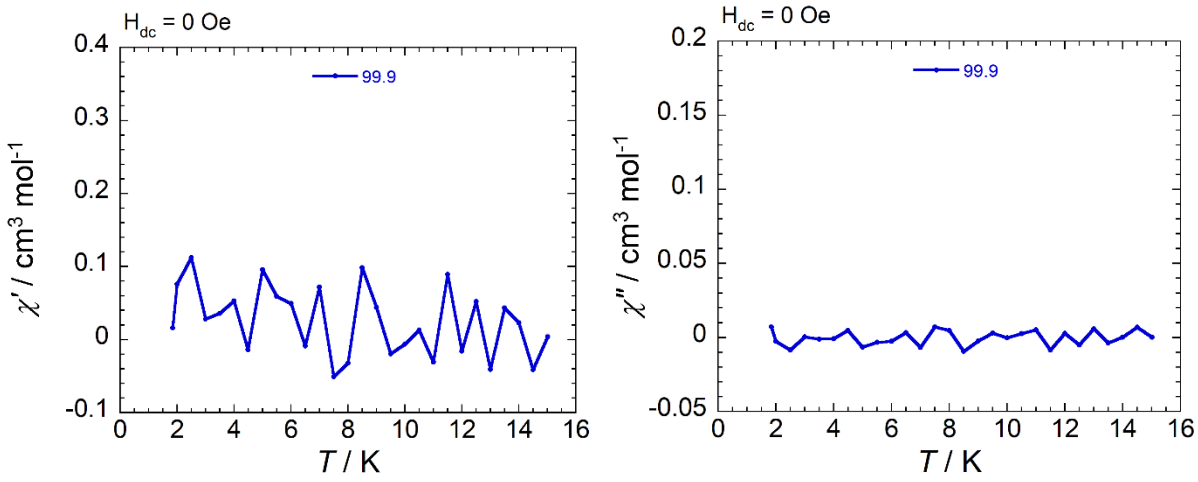

Fig. S39. Frequency (100 Hz) vs temperature plot of the real (χ', left) and imaginary (χ'', right) components of the ac susceptibility at 0 Oe external dc field and different temperatures from 1.8 – 15 K, respectively with a 3 Oe ac field for a polycrystalline sample of **3**.

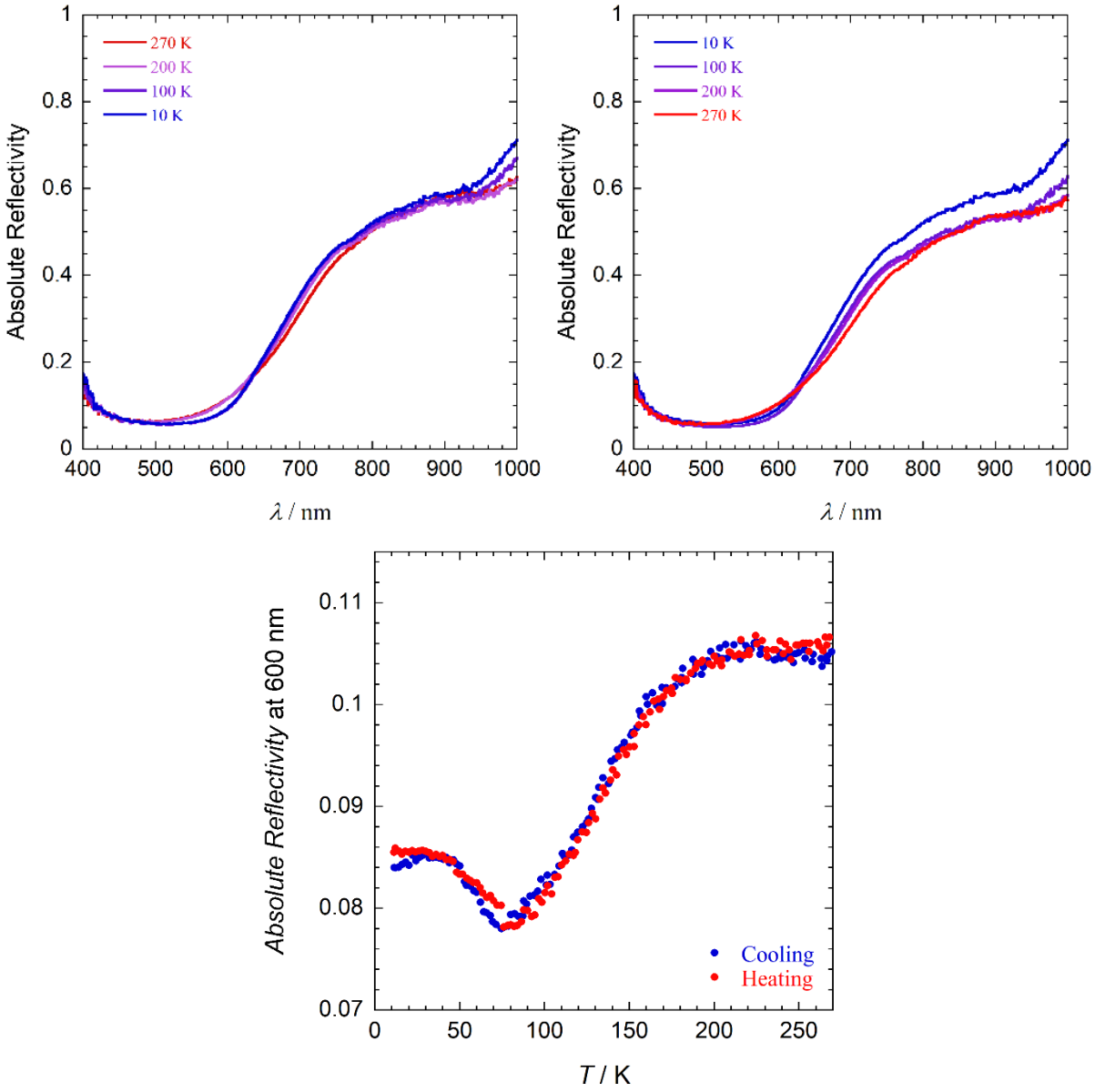

Fig. S40. Selected optical reflectivity spectra between 270 and 10 K recorded in the dark in cooling (top, left) and heating (top, right) mode and at a scan rate of 4 K min^{-1} for **3**. Bottom: thermal evolution of absolute reflectivity signal plotted at 600 nm in cooling mode (270 - 10 K, at 4 K min^{-1}, blue circle markers) and heating mode (10 - 270 K, at 4 K min^{-1}, red circle markers) in dark. A spectroscopic white light of 0.5 mW/cm² has been used for these measurements.

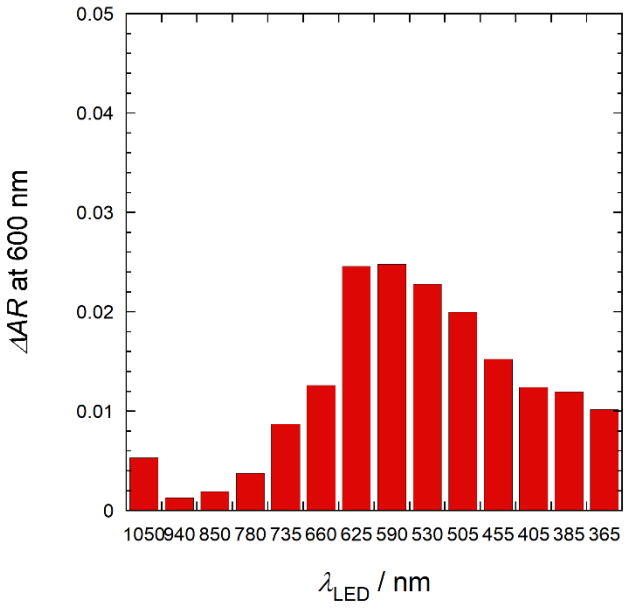

Fig. S41. Variation of the absolute optical reflectivity (ΔAR) plotted at 600 nm and 10 K (after a fast cooling of the sample from room temperature) before and after excitation with different LEDs (10 min, at 16 mW cm^{-2}) for **3**.

To explore the photo-sensitivity of **3** towards the LED light irradiation, the complex was cooled down to 10 K and irradiated with 590 nm LED (16 mw cm^{-2}) for 60 min. The resultant spectrum significantly differs from the spectra obtained in the dark for both 10 and 270 K (Fig. S38) confirm the formation of metastable HS Fe(II) state, at least on the surface of the sample. The evolution of absolute reflectivity as a function of time exhibits an increase in the absolute reflectivity value, attending a saturation value of around 20 min of white light irradiation. The value is similar to the one obtained at 270 K, which leads to a complete recovery of the HS spectra and thus suggests the spin-state switching between the diamagnetic LS (S = 0) state to paramagnetic HS (S = 2) state. After irradiation, the thermal stability of the photo-induced state was explored by heating the sample in dark (0.4 K min^{-1}), which shows a decrease in the absolute reflectivity due to the relaxation of the photo-induced state where complete relaxation was observed at 76 K (T_{LIESST}) (Fig. S39). After this temperature, the absolute reflectivity values show a similar feature as in the dark. This phenomenon suggests the complete reversibility after the photo-induced spin-state switching in sample **3**.

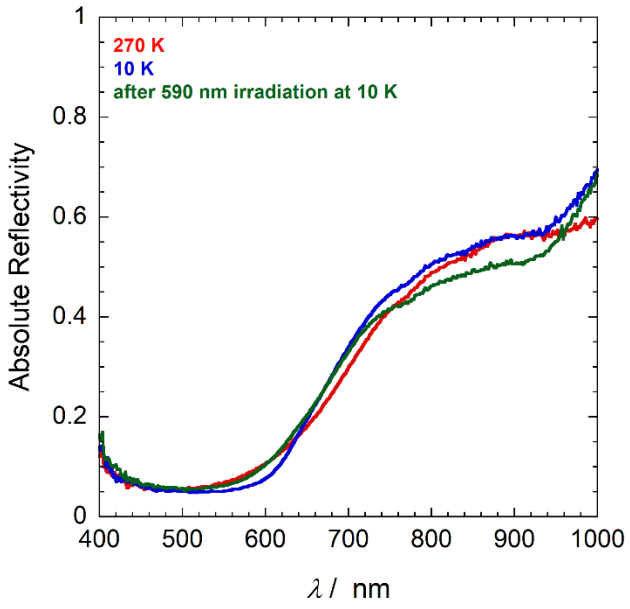

Fig. S42. Comparison of optical reflectivity spectra at 270 K (red), 10 K (blue) in dark and after 10 min of successive 590 nm (16 mW cm^{-2}) excitation (green) for **3**.

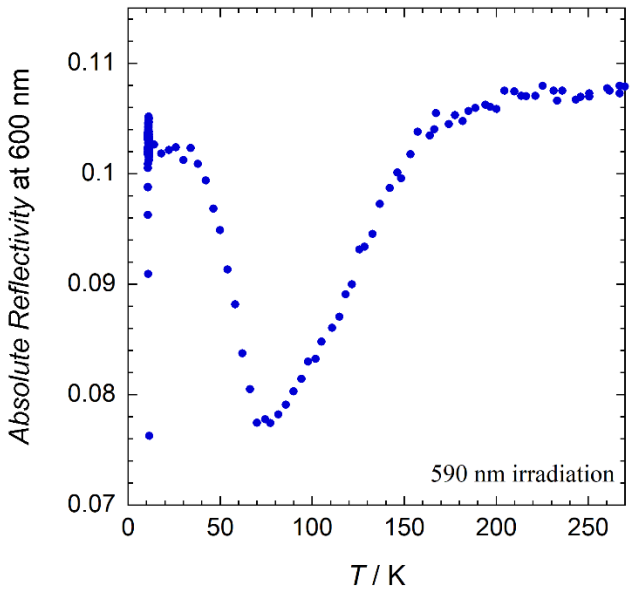

Fig. S43. Thermal evolution of reflectivity signal plotted at 600 nm during 590 nm irradiation (16 $mWcm^{-2}$, at 10 K) and in heating mode in dark (10-270 K, at 4 K/min, circle markers) for **3**.

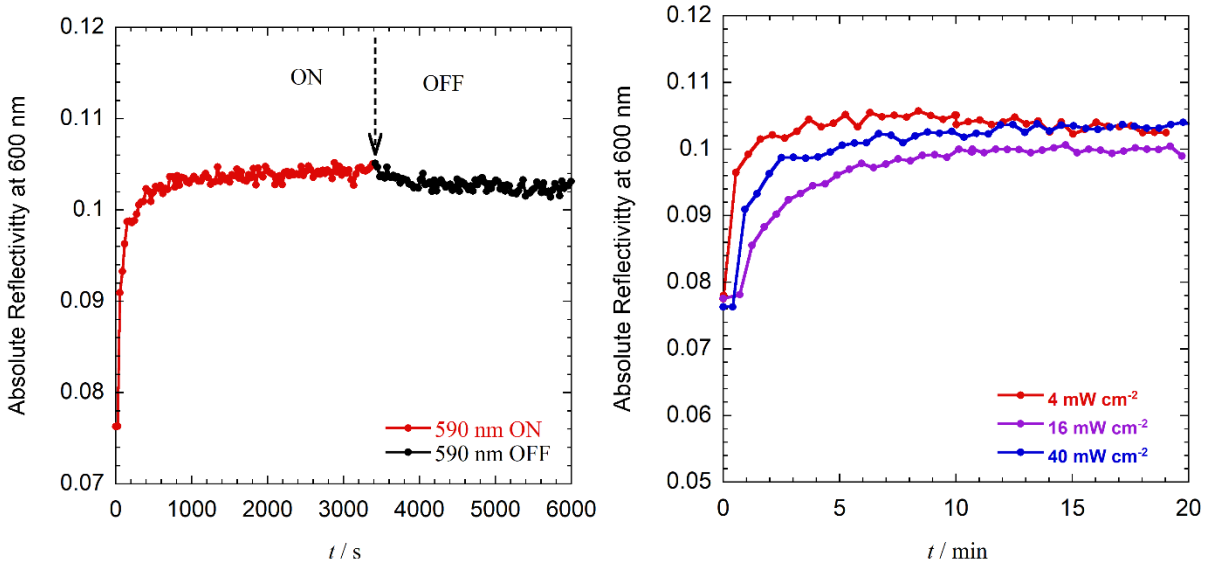

Fig. S44. Left: Time evolution of reflectivity signal plotted at 600 nm during ON and OFF of the irradiation at 590 nm (16 mW/cm^2) for **3**. A weak time relaxation of the photo-excitation that can be seen mainly the first 5 minutes, is then very slow, with a loss after 30 minutes of dR = 0.002 a.u. (for a photo-induced modification of 0.028 a.u.); Right: Time evolution of reflectivity signal plotted at 600 nm during the irradiation at 590 nm with different power for **3**.

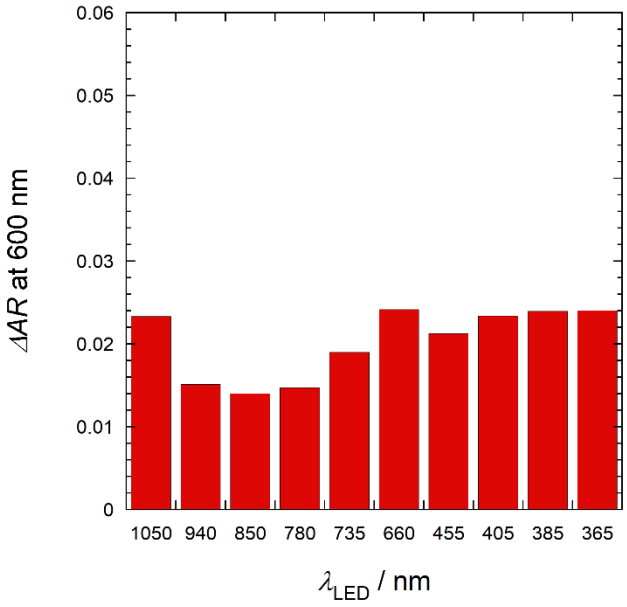

Fig. S45. Variation of the absolute optical reflectivity (ΔAR) plotted at 600 nm and 10 K, after first irradiation 590 nm LED (30 min, 16 mW cm^{-2} with successive second excitation with different LEDs (10 min, 16 mW cm^{-2}) for **3**.

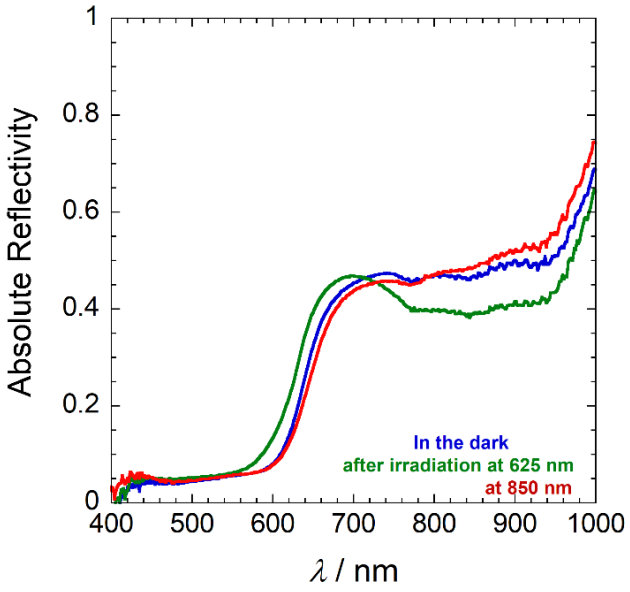

Fig. S46. Comparison of the surface-reflectivity spectra at 10 K (reached from 270 K at 4 K min^{-1} in the dark; blue) and after 10 min of successive 590 nm (16 mW cm^{-2}) (green) and 850 nm (120 $mWcm^{-2}$) (red) excitation for **3**.

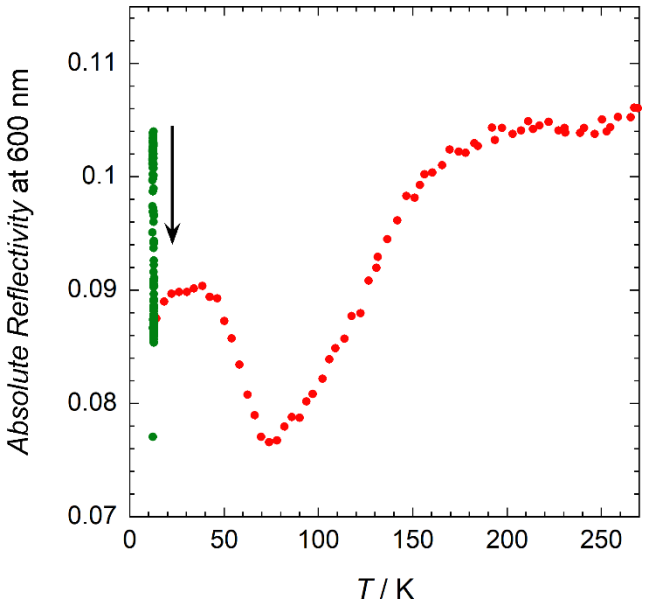

Fig. S47. Thermal evolution of reflectivity signal plotted at 600 nm after 850 nm irradiation (120 $mWcm^{-2}$, at 10 K, green circle markers) and in heating mode in dark (10-270 K, at 0.4 K/min, red circle markers) for **3**. Arrow indicates decreased in reflectivity during 850 nm irradiation.

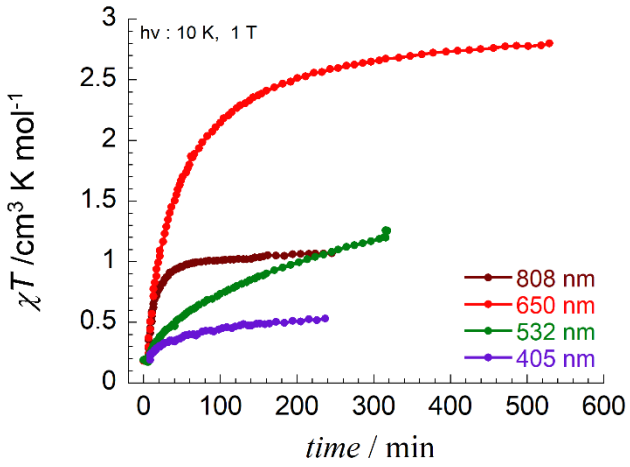

Fig. S48. χT *vs* time curves for **3** under 405, 532, 650, and 808 nm laser light irradiations at 10 K and 10000 Oe field.

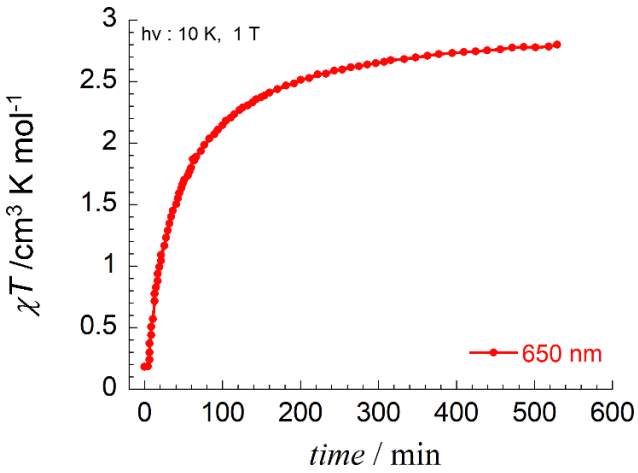

Fig. S49. χT *vs* time curves for **3** under 650 nm laser light irradiations at 10 K and 10000 Oe field.

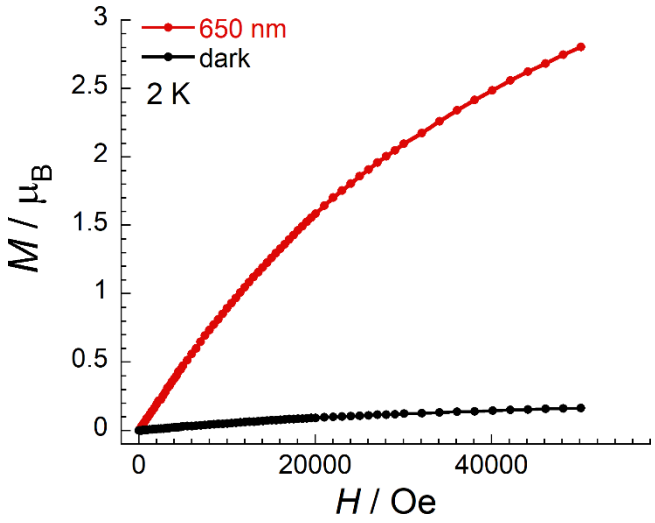

Fig. S50. M *vs* H curves of **3** after 650 nm light irradiation (red) and in dark (black) at 2 K.

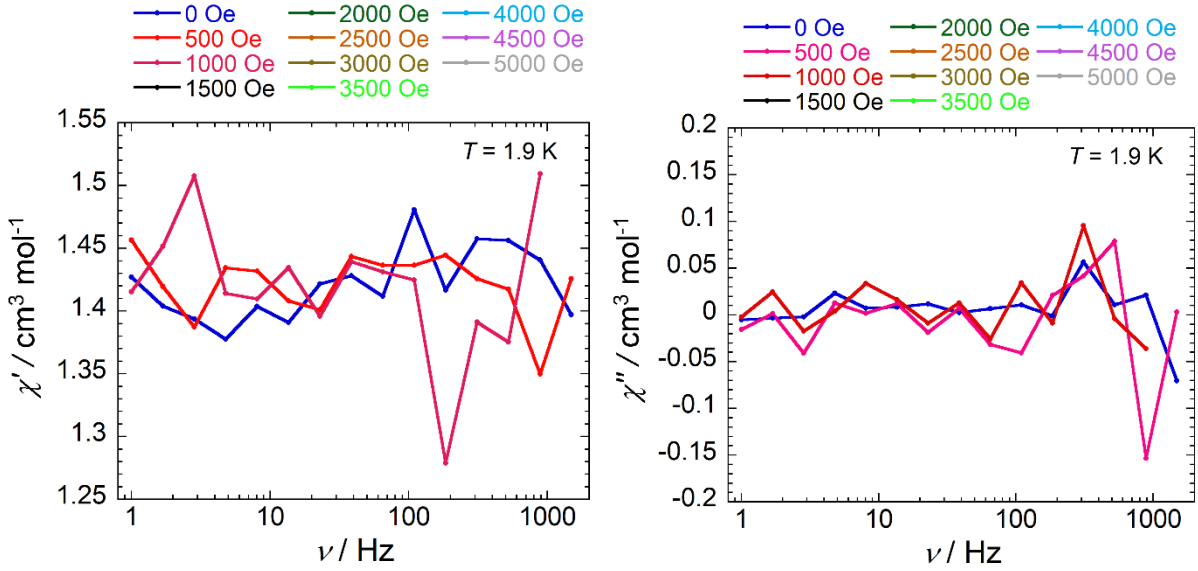

Fig. S51. Frequency dependency of the real (χ', left) and imaginary (χ'', right) components of the ac susceptibility under applied external dc field at 1.9 K with a 3 Oe ac field for a polycrystalline sample of **3** after 650 nm light irradiation.

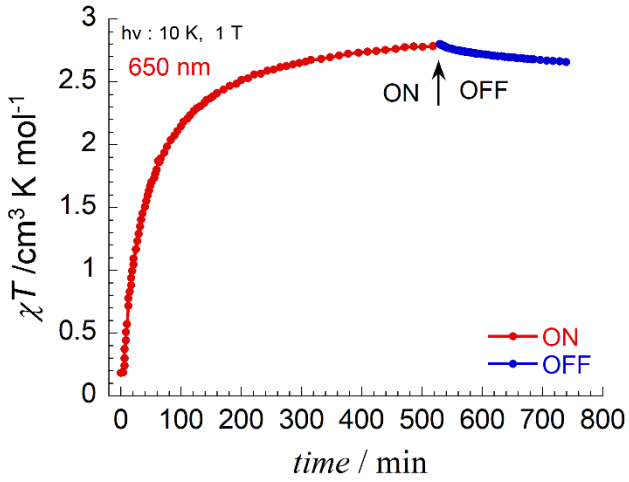

Fig. S52. χT *vs* time curves for **3** under 650 nm laser light irradiations at 10 K and 10000 Oe field during ON and OFF modes.

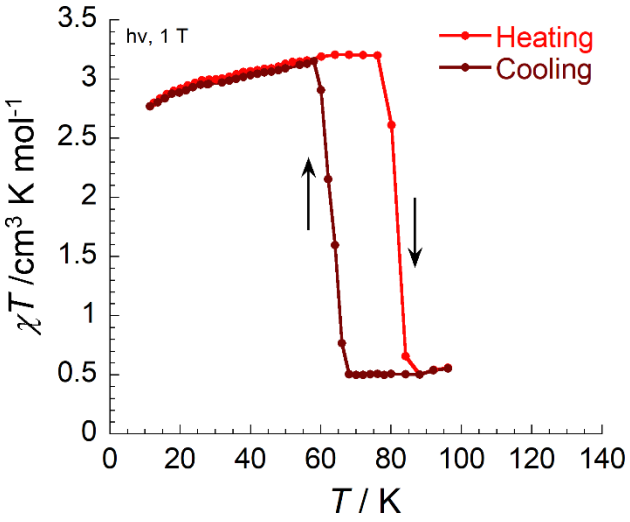

Fig. S53. χT *vs* T curves of **3** under continuous 650 nm light irradiation in heating and cooling modes with a sweep rate of 0.4 K min^{-1} at 10000 Oe field.

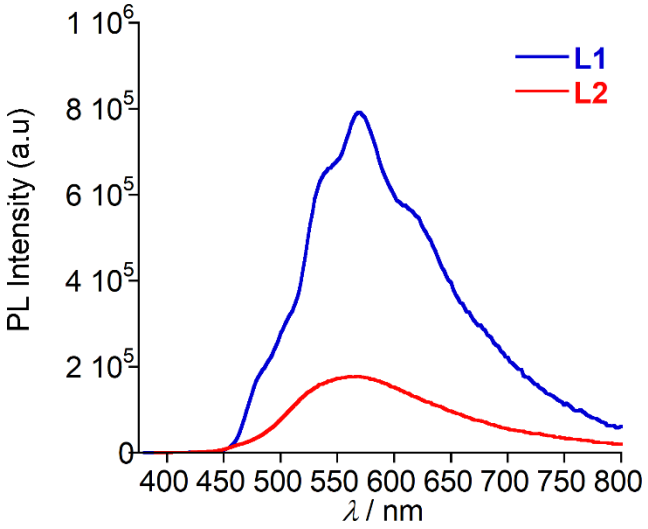

Fig. S54. Luminescence spectra of **L1** and **L2** at room temperature.

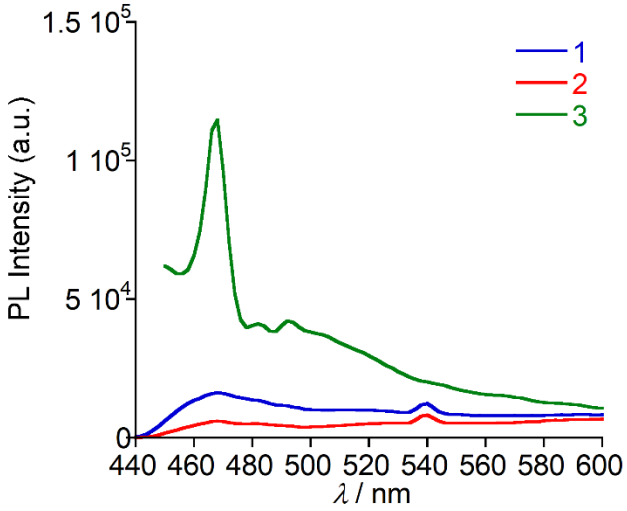

Fig. S55. Luminescence spectra of **1** - **3** at room temperature.

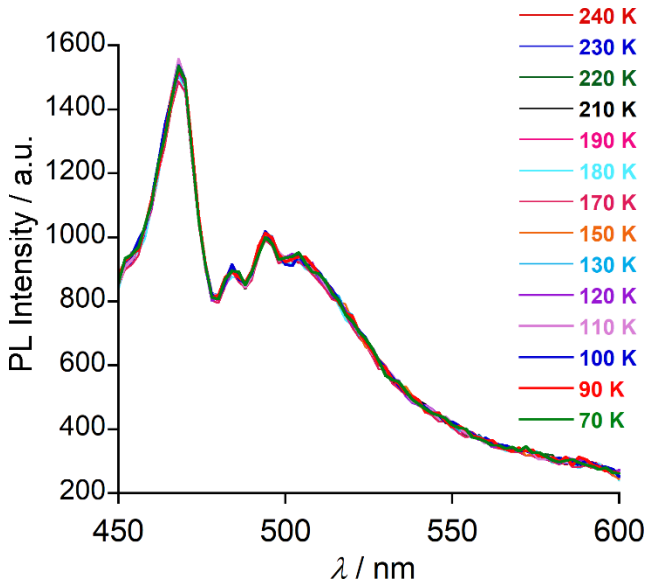

Fig. S56.Temperature dependence luminescence spectra of **3**.

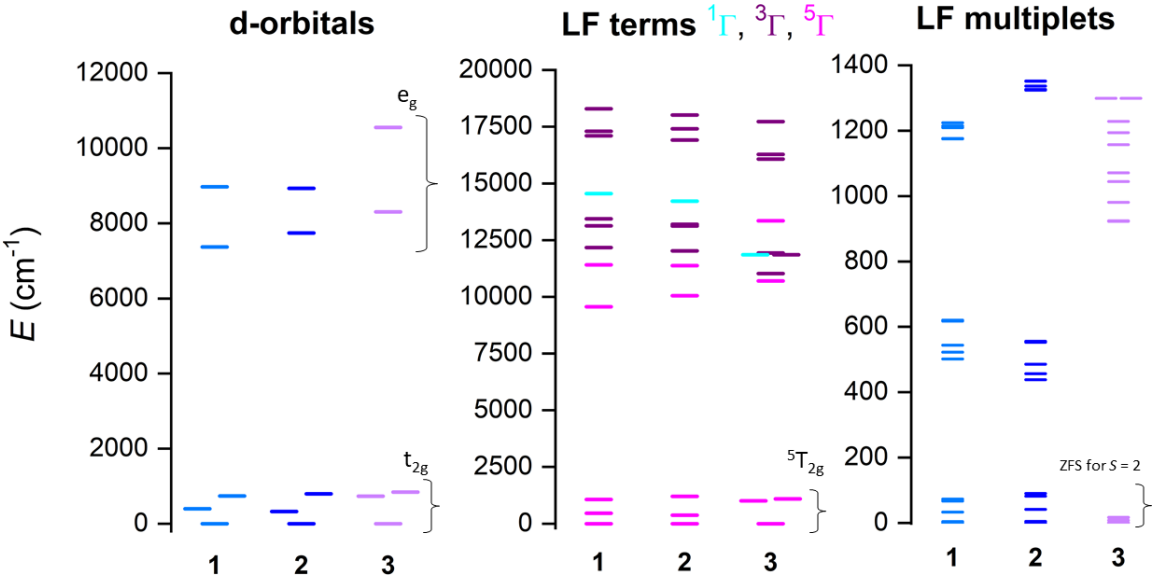

Fig. S57. The results of CASSCF/DLPNO-NEVPT2 for [Fe(**L1**)$_2$(NCS)$_2$(MeOH)$_2$] of **1**, [Fe(**L1**)$_2$(NCSe)$_2$(MeOH)$_2$] of **2** and [Fe(**L2**)$_4$(NCS)$_2$] of **3**. Left: the splitting of d-orbitals resulting from AILFT analysis; middle: the ligand field terms (LFT); right: the ligand field multiplets (LFM).

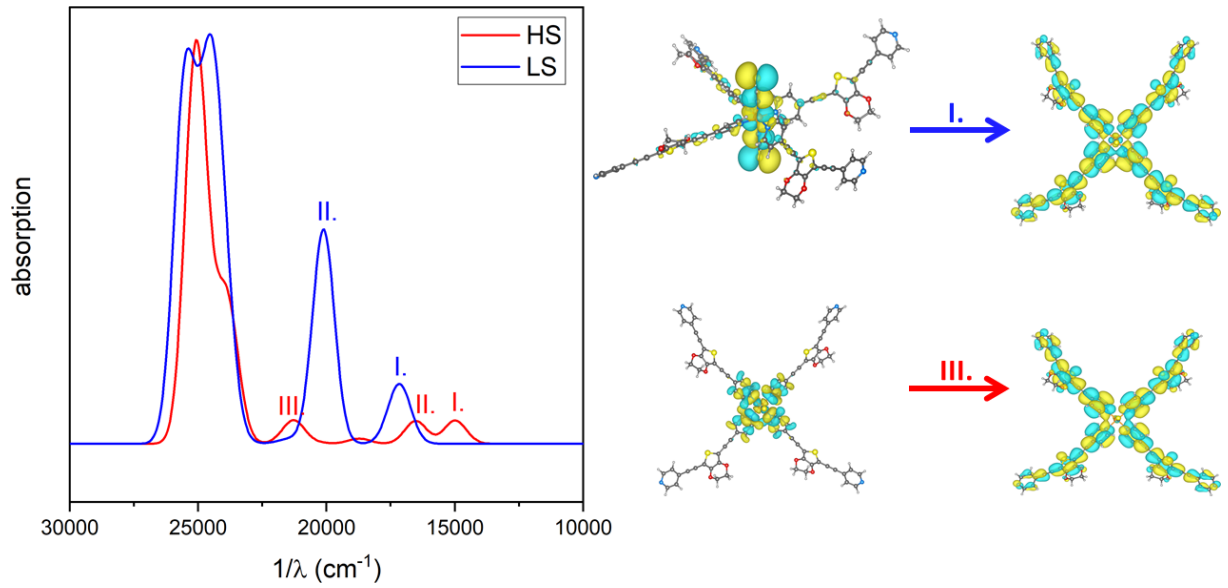

Fig. S58. Left: the TD-DFT calculated absorption spectrum of HS and LS spin isomers of **3**, [Fe(**L2**)$_4$(NCSe)$_2$] calculated with B3LYP functional. Right: selected Natural Transition Orbitals (NTO) for transition I.^{LS} and III.^{HS}, while all NTOs are depicted in Fig. S59.

Fig. S59. The Natural Transition Orbitals (NTO) calculated for LS and HS isomers of [Fe(**L2**)$_4$(NCS)$_2$] of **3** with TD-DFT using B3LYP functional on optimized molecular geometries.

LS isomer		
Wavenumber	From	To
17008.5	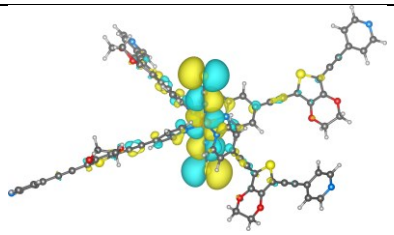	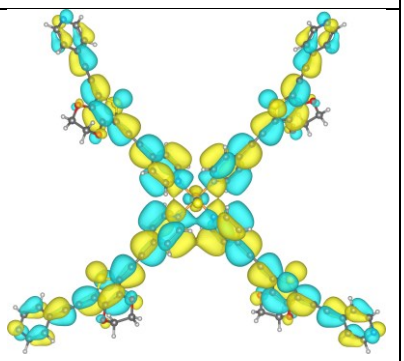
17032.6	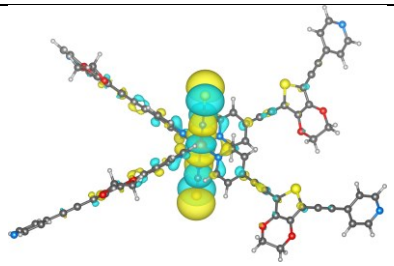	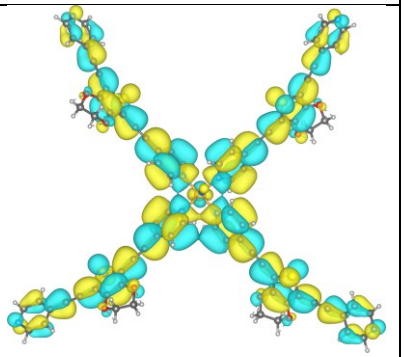
17260.5	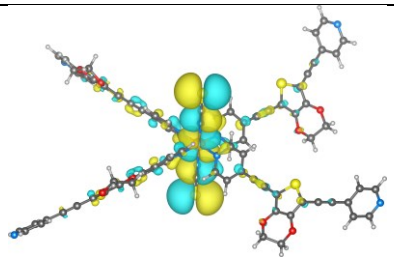	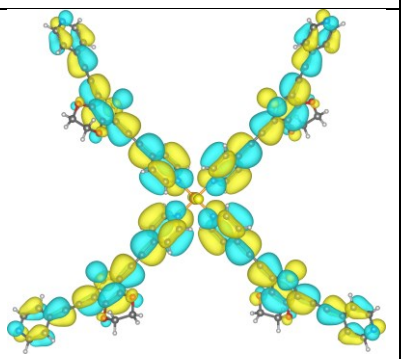

17284.8	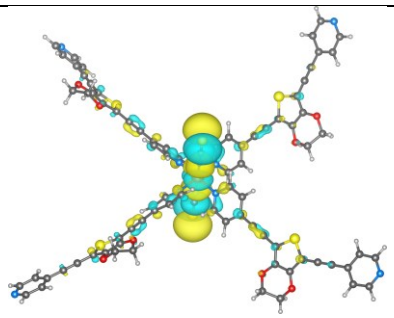	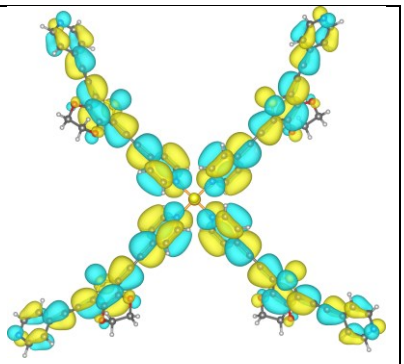
20109.6	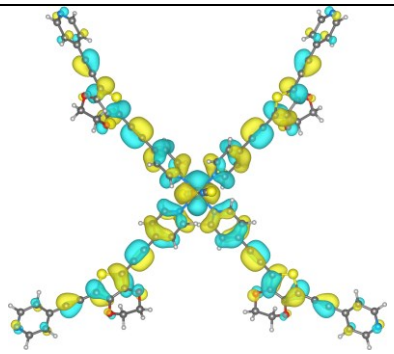	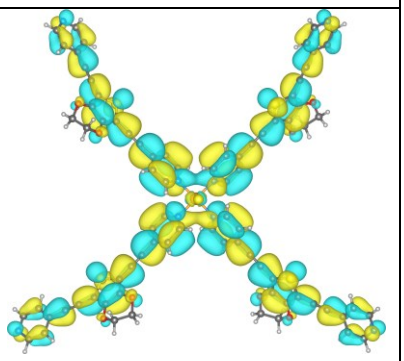
20121.0	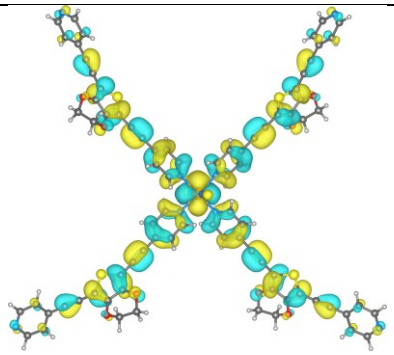	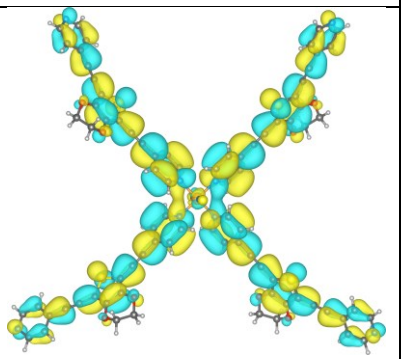
HS isomer		
Wavenumber	From	To

14866.1	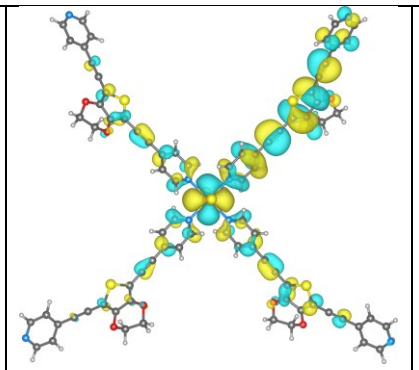	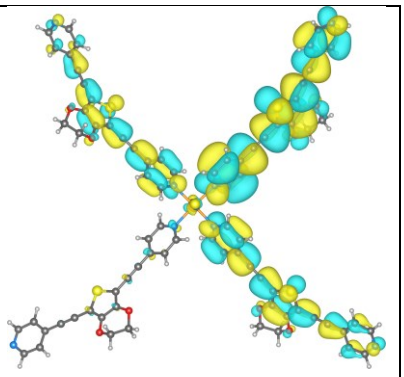
14980.9	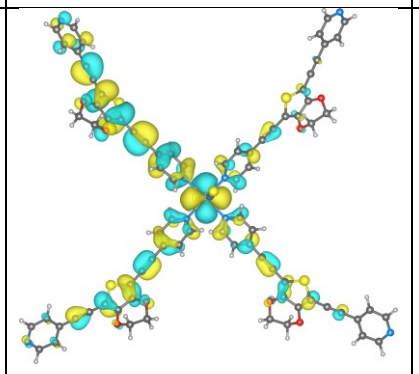	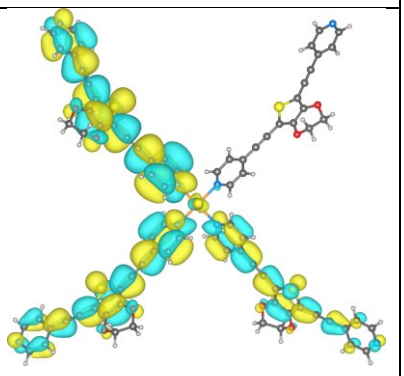
15065.0	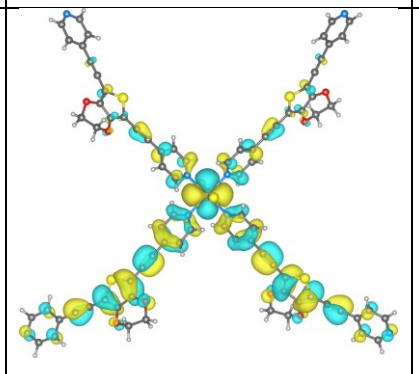	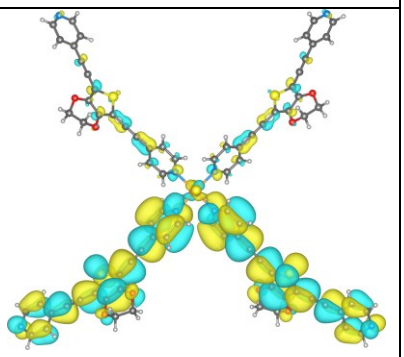
16486.8	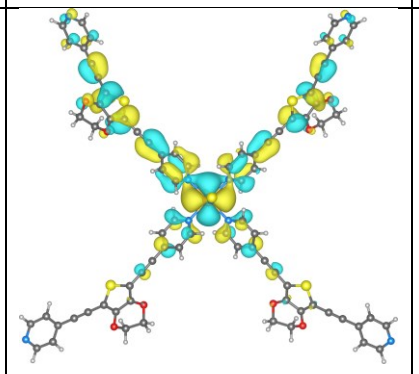	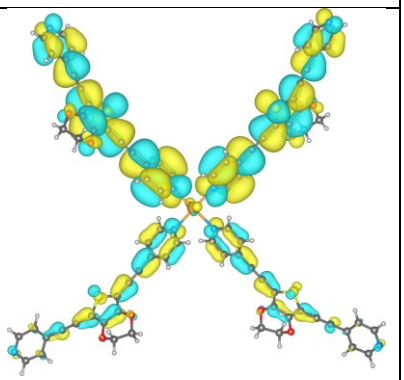

16573.7	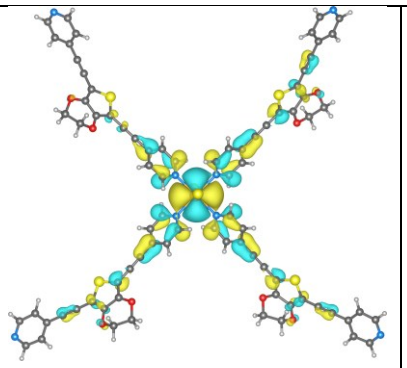	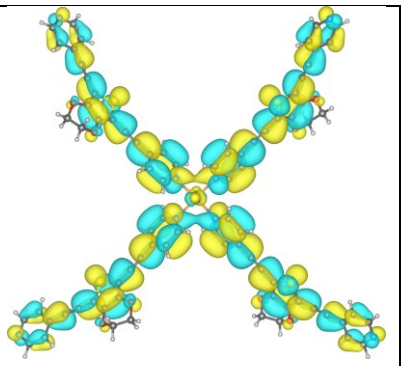
16465.0	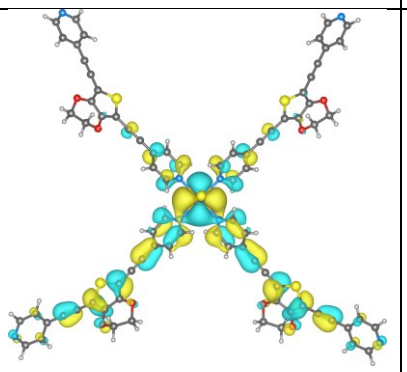	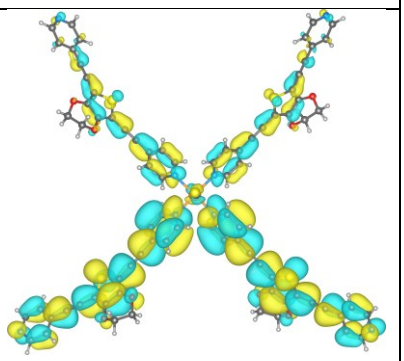
21120.2	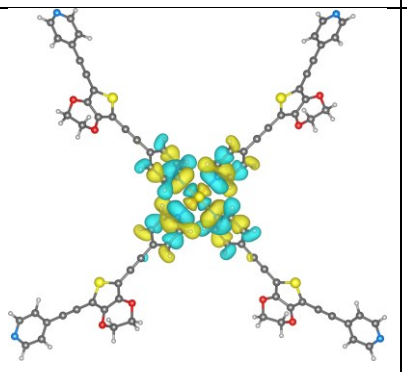	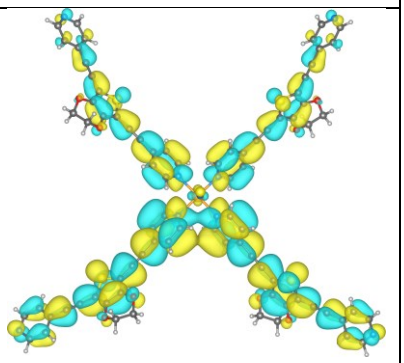
21213.4	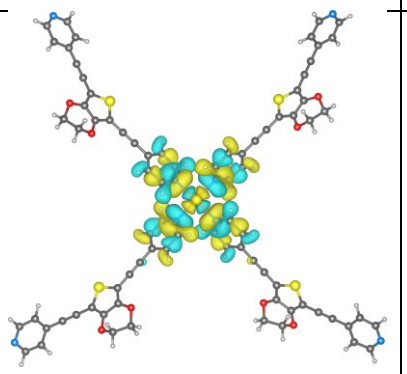	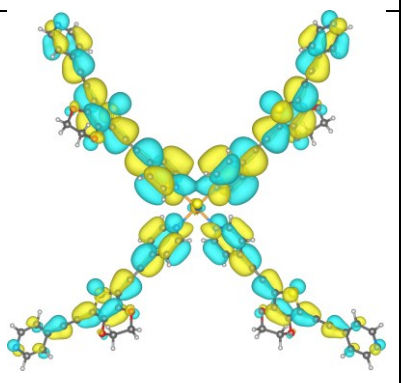

21471.5	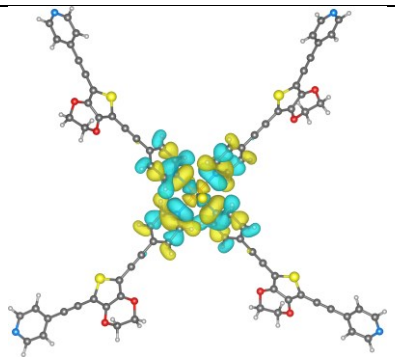	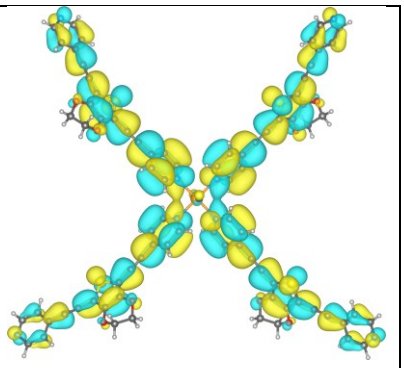

XYZ coordinated of B3LYP optimized geometry of LS isomer of [Fe(**L2**)$_4$(NCS)$_2$] of **3**:

Fe	-0.01443011126011	1.01654672788433	6.92292366541691
N	0.29110757161806	-0.42330304048040	8.30638540677665
N	-0.31977845977404	-0.41984199666267	5.53579539354267
N	0.28899575929801	2.43678693423625	8.32616679772016
N	-0.31725565660006	2.44002104462287	5.52280318813341
N	-1.91769816096112	1.02073084810553	7.33657641825519
N	1.88885029620198	1.02131075088927	6.50939877778519
C	-0.35154237239599	-0.40450374209627	9.48720486270983
C	1.13222584939338	-1.44335479219095	8.05937921605482
C	0.32404950378474	-0.39872449051845	4.35565661963772
C	-1.16030045731067	-1.44093078435347	5.78046645194157
C	1.35108190839936	2.37807853074616	9.14931106424706
C	-0.57081283514162	3.46017626095656	8.47452459417455
C	-1.37829285713730	2.38246821610949	4.69824566445331
C	0.54337639547171	3.46299253037479	5.37616821398494
C	-3.06129076213718	1.02751064891293	7.57635969900796
C	3.03245544547252	1.02814437898141	6.26968681241480
C	-0.18710049054507	-1.38649956582314	10.45380563108060
H	-1.02611085147782	0.43308553611059	9.65631397813634
C	1.35814864730801	-2.47288998202850	8.96044708308741
H	1.64178150756076	-1.42709406170971	7.09802959521032
C	0.16183381609382	-1.37973236031259	3.38770927362973
H	0.99775605455231	0.43988510336118	4.18823689536371
C	-1.38409649160775	-2.46960522136631	4.87786683682257
H	-1.67103361612869	-1.42624870275823	6.74122537802080
H	2.03126331071243	1.54151835021633	9.00030991569305
C	1.59310600956423	3.31796250123915	10.14063395287726
C	-0.41094880832208	4.45002824674021	9.43346232323701
H	-1.42188726112453	3.47840524217915	7.79605610356158
H	-2.05937934344374	1.54644978035216	4.84620152381827
C	-1.61805756093205	3.32265799300685	3.70663846345397
C	0.38575083088632	4.45307904264021	4.41711435952589
H	1.39334681575179	3.48062418233668	6.05602813541444
S	-4.66846619985259	1.03662809873253	7.91053779371322
S	4.63964697101287	1.03730485571388	5.93565449255256
C	0.68807160211741	-2.46377907165457	10.20187366664554
H	-0.73376202893200	-1.31895999969128	11.39498358225687
H	2.04937968270826	-3.27673303811003	8.70448431894946
C	-0.71241128246549	-2.45830818777353	3.63734097414056
H	0.70947912960929	-1.31044107708263	2.44723043596162
H	-2.07483500300621	-3.27444838747139	5.13201201251631
C	0.69695330580819	4.39514851951436	10.30525095897588

H	2.46996928678600	3.21820985996520	10.78145420239564
H	-1.13980449627417	5.25796295248629	9.50687377950167
C	-0.72068105369251	4.39901539861156	3.54338047468463
H	-2.49405370542871	3.22368881985967	3.06451202078869
H	1.11529446170060	5.26051100338961	4.34499393710499
C	0.89200958488494	-3.49599325129712	11.15389227362262
C	-0.91350037839148	-3.48967262593612	2.68382586128638
C	0.90317673910173	5.38257872312810	11.30357919490973
C	-0.92395652548122	5.38637548987890	2.54436418322693
C	1.07938542918247	-4.38966270986107	11.96710556879595
C	-1.09798830826669	-4.38259364886931	1.86913822892363
C	1.08627109441321	6.23439763228973	12.16162784699165
C	-1.10405379033683	6.23840567542763	1.68588534236943
C	1.30073107189017	-5.40710413352207	12.90372018633253
C	-1.31515351975449	-5.39919925000716	0.93066555122519
C	1.30284861916337	7.21664470977442	13.13656309016147
C	-1.31698020800384	7.22094628013408	0.71042592335663
C	2.07674413840002	-6.55288170419393	12.74340807259759
S	0.57999172900559	-5.36902312369057	14.49405281760367
C	-2.09128252350437	-6.54553599686736	1.08640179316139
S	-0.58826030075234	-5.35859095917937	-0.65679445506309
C	2.33201475345075	7.26604398203529	14.07409004809526
S	0.26753515581933	8.61593806774013	13.28448902118503
C	-2.34325194096138	7.27154824466530	-0.23022279498718
S	-0.27987006486221	8.61924009467121	0.56592381074358
C	2.09731847219093	-7.38098994096833	13.90052920534589
O	2.75578789733397	-6.85383172302816	11.61420024018499
C	1.32753949015567	-6.87995232217062	14.94696393627834
C	-2.10685350271393	-7.37208746759038	-0.07192740600691
O	-2.77472244690206	-6.84829501413321	2.21248696808892
C	-1.33305837615948	-6.86935743119389	-1.11458494481415
C	2.27884004016308	8.42112729052702	14.90323415096349
O	3.28878317605729	6.31933542280234	14.19710585165917
C	1.21564102169138	9.26679007537895	14.59791447935921
C	-2.28623889064076	8.42664134888362	-1.05913396153362
O	-3.30067149832827	6.32589041784340	-0.35625580825406
C	-1.22304963869046	9.27111980398317	-0.75049584728038
O	2.79986691641420	-8.53489584058835	13.96321987537923
C	3.20497977835819	-8.23096135269220	11.57762877557013
C	1.15713599393418	-7.43561024207506	16.22254327586335
O	-2.80871243919597	-8.52614735448670	-0.13905795154058
C	-3.22341976390718	-8.22568903327127	2.24536141467575
C	-1.15724439573224	-7.42328143562979	-2.39018676459341
O	3.18198930366820	8.66612777147544	15.87918476766727

C	4.42243570700509	6.76544144135079	14.98216314461592
C	0.89355212001808	10.48052046143964	15.22091237957449
O	-3.18608332681820	8.67266607157117	-2.03788613704027
C	-4.43132024550563	6.77316714759801	-1.14496789518587
C	-0.89750503658439	10.48452592850789	-1.37235447670289
C	3.79058779423871	-8.64209946045672	12.91139903823282
H	2.34937310883918	-8.87278858839326	11.31049493127743
H	3.96586550685189	-8.28502729371703	10.78873141442676
C	1.01524295181156	-7.91155712946327	17.33942012769162
C	-3.80351146127806	-8.63526421511413	0.90869899629827
H	-2.36856969345084	-8.86746719925521	2.51502265372249
H	-3.98743689578806	-8.28120537420761	3.03112509939788
C	-1.01088703840789	-7.89776575520224	-3.50710990557942
C	3.96424447491530	7.49688298218847	16.22574335851849
H	5.05074017005281	7.41630079257801	14.35228186062767
H	4.98347237548467	5.86199594346247	15.25249345040455
C	0.62666064717945	11.54112351432911	15.76689685279979
C	-3.96839392786154	7.50422677635177	-2.38702113699179
H	-5.06101325272715	7.42459625627834	-0.51706723061729
H	-4.99236796063772	5.87028907827133	-1.41716178107868
C	-0.62759845835765	11.54482730060902	-1.91744836845741
H	4.65242036229501	-8.00649717638153	13.17385486161334
H	4.10176896347120	-9.69408001367827	12.88784925946842
C	0.85819708399584	-8.46220951708223	18.64104191407048
H	-4.66460360303938	-7.99971643683395	0.64369066417165
H	-4.11427201834281	-9.68742702846132	0.92956622228732
C	-0.84848989877276	-8.44706306457755	-4.80864608451999
H	3.35070758392902	6.83955903153182	16.86340850217464
H	4.82682957545170	7.86296399303426	16.79671666708006
C	0.33442880238854	12.77630212744207	16.40807926657566
H	-3.35347908191292	6.84632658286896	-3.02276108596462
H	-4.82877198956180	7.87119572190680	-2.96074616773728
C	-0.33189946926376	12.77970113440346	-2.55765135861478
C	0.15672906201787	-7.76939856512783	19.64967795548822
C	1.40092261624280	-9.72113165829830	18.97254758314344
C	-0.14297181989392	-7.75319409102774	-5.81372325612962
C	-1.38964071563184	-9.70576640749212	-5.14355062572345
C	1.19898763882353	13.30965451999882	17.38675071220110
C	-0.82466860967337	13.51455311401379	16.09120802583316
C	-1.19224219872408	13.31363926733715	-3.53971808806748
C	0.82663431056626	13.51699650652132	-2.23649541864624
H	-0.28353420220823	-6.79118922352867	19.45027433773551
C	0.03672232869788	-8.35662568223384	20.90713488792894
C	1.21844393554631	-10.21085320413466	20.26375362332090

H	1.95317185831615	-10.30166438850492	18.23181913553296
H	0.29636047401470	-6.77512683874939	-5.61158322668180
C	-0.01779988327078	-8.33917875940140	-7.07125996913954
C	-1.20192696609505	-10.19416480020439	-6.43450723938094
H	-1.94475193026631	-10.28711349656091	-4.40560568277069
H	2.11009332423508	12.78108677240045	17.67159346785775
C	0.86918476389529	14.52455264618936	17.98272619321593
H	-1.53004585361853	13.15040839913565	15.34251177593333
C	-1.05407206339530	14.71865013096629	16.75315610964957
H	-2.10271078305777	12.78581275714583	-3.82794939293890
C	-0.85906967380856	14.52812685922472	-4.13466449598000
H	1.52882615861962	13.15238205720784	-1.48503742947181
C	1.05964317397070	14.72075717018912	-2.89779737988580
H	-0.50438073284982	-7.83299733819841	21.70227054729287
N	0.55208789146340	-9.55254751465261	21.22154502632027
H	1.63187997296387	-11.18693358209820	20.53844381064821
H	0.52641859391266	-7.81468970815909	-7.86370068842636
N	-0.53179304084526	-9.53482216133975	-7.38894177223528
H	-1.61406216231462	-11.17005390899062	-6.71181935858581
H	1.52978576174949	14.95368973525592	18.74353523136369
N	-0.23200316611279	15.22557862646326	17.68147767365141
H	-1.94941845909096	15.30486011350566	16.52081723934225
H	-1.51637233977737	14.95771350135044	-4.89807242370379
N	0.24160481408488	15.22821742380520	-3.82937314610410
H	1.95462072349477	15.30620997780235	-2.66214857075486

XYZ coordinated of B3LYP optimized geometry of HS isomer of [Fe(**L2**)$_4$(NCS)$_2$] of **3**:

Fe	6.88943638107909	1.07645919797027	7.04037061863739
N	4.84734165224154	1.09512891346867	7.51844976143815
N	8.93133988921874	1.09398895839548	6.56379226141791
N	6.51829743341826	-0.52851774616422	5.52987933694154
N	7.25833034183439	-0.52551608101256	8.55427359576839
N	6.53174384085028	2.64380699909194	5.48721198226200
N	7.24635866982802	2.64537388491568	8.59417409453797
C	3.69453467459926	1.20604107481817	7.70325820964472
C	10.08376865022828	1.21157905627027	6.38053938527410
C	7.14868462627699	-0.52754206778507	4.34731083042890
C	5.69436259546771	-1.54695727295163	5.81494082729212
C	6.62653191630621	-0.52207799132554	9.73608326493828
C	8.08244939325117	-1.54459204147346	8.27213501495416
C	7.37017943978940	3.68099435580999	5.35133792460133
C	5.48486341078409	2.55454214648058	4.65444088771784
C	6.40388956135183	3.67892733562469	8.73295484169001

C	8.29013535121508	2.55455398981506	9.43058548061003
S	2.09176424691571	1.36935939452879	7.96757276850999
S	11.68846930144112	1.37601332330608	6.12889063233537
C	6.99005594031310	-1.53575056444202	3.40457361888710
H	7.81055243293444	0.31860392320432	4.15342470468954
H	5.19801941691766	-1.50916727865515	6.78597368391711
C	5.46747410576055	-2.60343853763512	4.94296027783866
C	6.78421580902169	-1.52822979710287	10.68113165020143
H	5.96428940811572	0.32434839043547	9.92735494026206
H	8.57972853780010	-1.50884631349534	7.30149885404109
C	8.30847685532579	-2.59921036435009	9.14662222453646
H	8.21078402107505	3.71773266438206	6.04663818303217
C	7.20450940971019	4.66662521827421	4.38650063695674
C	5.22977299712743	3.48661882474597	3.65659901368324
H	4.82490117000020	1.69730089239884	4.79800082526513
H	5.56619170728021	3.71740004039471	8.03424208929926
C	6.56181305922354	4.65862899592240	9.70506532412968
C	8.53746761629817	3.48075953723315	10.43592644117374
H	8.95387275554268	1.70071206739896	9.28409325105266
C	6.12784950971581	-2.61455874211913	3.69556429022975
H	7.52526486131397	-1.49003577251287	2.45536547336123
H	4.78867331199235	-3.41048108219430	5.22167532840403
C	7.64685219187921	-2.60756759276701	10.39336062641783
H	6.24793056061693	-1.48060869198301	11.62963772409518
H	8.98750706940089	-3.40687850471668	8.87028653136310
H	7.91389020198359	5.49218890731899	4.31638095117019
C	6.10655795407345	4.58216061609683	3.50341369201598
H	4.36452602927894	3.36950119816538	3.00279969491068
H	5.84923077267533	5.48123302014319	9.77751832117063
C	7.65579547354923	4.57182230259934	10.59289099699679
H	9.40032689251603	3.36232539930360	11.09263969891902
C	5.92828533356777	-3.67166206811919	2.76905748246229
C	7.84572117062953	-3.66224755624976	11.32274650311687
C	5.89028265791151	5.56397944476901	2.50059663242495
C	7.86239199899672	5.54702489398587	11.60423254039382
C	5.74836270081126	-4.58279909139222	1.97389312098116
C	8.02445037905368	-4.57120332960606	12.12066959346298
C	5.69917911868660	6.41122256543645	1.63993175129697
C	8.04216297986941	6.38876478869089	12.47272696113969
C	5.53939156875673	-5.61769279213155	1.05351209884715
C	8.23174699320841	-5.60261312497302	13.04530942569813
C	5.47392825170589	7.38906059258445	0.66239452580145
C	8.25005082212491	7.36238620778480	13.45835357389010
C	4.77169431261376	-6.76700357633347	1.22695854696775

S	6.27042671908905	-5.59893478437667	-0.53250799857655
C	8.99785132320496	-6.75378768584423	12.87728711604761
S	7.50166831256367	-5.57479956941942	14.63161171259940
C	4.44333355903450	7.42884096128525	-0.27390500469968
S	6.49901315116393	8.79524731873661	0.51002304615212
C	9.26593279302738	7.40233415030931	14.41055476341757
S	7.21696769208685	8.76377100087758	13.60106924338064
C	4.76688143189243	-7.61426877625553	0.08349217841797
O	4.08630683294239	-7.05514484628534	2.35565710638222
C	5.53944328008917	-7.12359259669513	-0.96572762003023
C	9.00271189050253	-7.59489263827531	14.02532749687566
O	9.68198439397897	-7.04867728150094	11.74955541584666
C	8.23132251385832	-7.09786408748177	15.07243961625612
C	4.48731337007908	8.58241308150611	-1.10579998137866
O	3.49295716520149	6.47529951853408	-0.39337924109974
C	5.54509118551024	9.43605135527757	-0.80395312612782
C	9.20391111765513	8.55178706439754	15.24715992636084
O	10.21867646686096	6.45240760382996	14.54053460083424
C	8.14732370613561	9.40236539206173	14.93291773550058
O	4.07553274188948	-8.77558306884588	0.03490429778218
C	3.64976326486849	-8.43570854916280	2.41215175601236
C	5.72291724738949	-7.69857522577163	-2.23088591925550
O	9.69338241700437	-8.75632696935299	14.07971937357587
C	10.11774335876214	-8.42975109278156	11.70039381766833
C	8.04813051060457	-7.66514811968560	16.34112411169053
O	3.58127099485295	8.81884237129157	-2.08118252749251
C	2.35541645486894	6.91138148966477	-1.17841918787817
C	5.85861174130561	10.64982333322552	-1.43125245923266
O	10.09343251981635	8.78758887121393	16.23775484345114
C	11.34250245353998	6.89090251150309	15.34373537083258
C	7.81764925603567	10.61192981211647	15.56012770767780
C	3.07819742291399	-8.87485182415104	1.08119387217968
H	2.88339556325530	-8.48371769628801	3.19613022539182
H	4.50929066046126	-9.06476907439290	2.69653395446043
C	5.87445515464347	-8.19125092616616	-3.33918887079085
C	10.68997915693045	-8.86183241114505	13.03335940330726
H	10.88353326125253	-8.48253222000969	10.91615572091387
H	9.25766316329248	-9.05991262509250	11.42013105054846
C	7.89520480594221	-8.15000933828054	17.45269004737957
C	2.80699501925341	7.64327977509052	-2.42414986893607
H	1.80068750631273	6.00327009237264	-1.44615862593313
H	1.72294180161512	7.55907162447715	-0.54944279694626
C	6.11754566157532	11.70971811315838	-1.98235622322401
C	10.86921512495462	7.61465323953626	16.58619540259333

H	11.89818156622243	5.98453278582459	15.61534374306403
H	11.98043869067220	7.54473014329138	14.72673322807814
C	7.54148838394054	11.66823504046734	16.10979411080130
H	2.77714902278216	-9.92931874311509	1.12026730776208
H	2.21210932738673	-8.25236027123556	0.80181992881878
C	6.04132109555033	-8.76147242777390	-4.63111730303651
H	10.99053314336681	-9.91663129405878	12.99990800070512
H	11.55649484456795	-8.23815962263536	13.30875373610346
C	7.72509635236594	-8.71194706554441	18.74783366089353
H	1.94117427862778	8.00180212526648	-2.99502259278386
H	3.42448245149575	6.98887563087553	-3.06102425508538
C	6.40039902815116	12.94408360620675	-2.62925427913605
H	11.72485614965451	7.97522721280937	17.17097043962020
H	10.24641201166607	6.95397368030407	17.21130159280348
C	7.23541001152167	12.89797506293377	16.75502794674091
C	6.74449949957814	-8.08105141029441	-5.64696897915205
C	5.50642026211889	-10.02811887275832	-4.94551892597548
C	7.01964645891304	-8.02473199599589	19.75753724795271
C	8.25876834829750	-9.97672198004761	19.07170941579381
C	7.55821920197838	13.68828261067229	-2.32191045517575
C	5.52745957874595	13.47054803853695	-3.60418882632451
C	6.08067234824870	13.63617867347990	16.42233430644977
C	8.08016892492667	13.42543227401964	17.75392812223428
C	6.87368874161973	-8.68729981758000	-6.89444621438208
H	7.17901426465534	-7.09768423857813	-5.46077842693923
H	4.95326822917963	-10.59971119494433	-4.19852632732452
C	5.69771273600792	-10.53704837231759	-6.22796923630717
C	6.88702153717598	-8.62294849879810	21.00852896677367
H	6.58604688397092	-7.04239711722648	19.56391581223984
H	8.81362819706199	-10.55324887358361	18.32979935783457
C	8.06396395386364	-10.47737303479360	20.35690394030224
H	8.26969486192854	13.32948980553585	-1.57640372737152
C	7.77838027656123	14.89118250928765	-2.98915120581833
C	5.84837653881563	14.68486464489874	-4.20613849374889
H	4.61682082333118	12.93720353462143	-3.88151041970762
H	5.39034427229447	13.27646883679974	15.65763876277746
C	5.83586415219493	14.83428068859576	17.08960278036701
C	7.73617544481268	14.63467787109644	18.35343187303114
H	8.98703090297108	12.89667424027633	18.05167436041156
H	7.41625367876533	-8.17354131772895	-7.69500744246633
N	6.36557213503680	-9.89045062547765	-7.19266087446073
H	5.29036602766458	-11.51932792349586	-6.48932750070732
H	6.34265206637076	-8.10384745978142	21.80441383528002
N	7.39385056334032	-9.82438228340656	21.31570701859517

H	8.47023026569457	-11.45810558178866	20.62562348691334
H	8.67262507236065	15.48196251140680	-2.76427297462435
N	6.94839843343578	15.39155342675521	-3.91398062350196
H	5.18121444715577	15.10869374300089	-4.96419552803132
H	4.94352986454539	15.42019982212462	16.84523424344101
N	6.63902158883775	15.33550586687353	18.03735128231792
H	8.38129523447540	15.05909903446535	19.13000216192577

Tables

Table S1. X-ray crystallography data for complexes **1** - **3**.

Complex	**1**	**2**	**3**	
CCDC no	2020246	2042421	2020247	2020248
Temperature, K	120	120	200	90
Empirical formula	$C_{36}H_{32}N_6O_6S_4Fe$ + solvent	$C_{36}H_{32}N_6O_6S_2Se_2Fe$ + solvent	$C_{42}H_{24}N_6O_4S_4Fe$ + solvent	$C_{42}H_{24}N_6O_4S_4Fe$ + solvent
Formula weight	828.76	922.56	860.76	860.76
Crystal system	Monoclinic	Monoclinic	Orthorhomic	Orthorhomic
Space group	*I 2/a*	*I 2/a*	*Ccca*	*Ccca*
a, Å	19.6279(4)	19.7511(6)	13.6023(7)	13.5275(6)
b, Å	7.7600(2)	7.8183(2)	28.4252(15)	28.0006(13)
c, Å	26.5705(6)	26.7494(7)	28.3740(13)	27.7775(16)
α, °	90	90	90	90
β, °	95.245(2)	96.254(2)	90	90
γ, °	90	90	90	90
V, Å^3	4030.07(16)	4106.1(2)	10970.8(10)	10521.5(9)
Z	4	4	8	8
d_{cal}, g cm^{-3}	1.366	1.492	1.042	1.087
μ, mm^{-1}	0.632	2.291	0.464	0.484
F(000)	1712	1856	3520	3520
θ max	27.481	27.483	27.484	27.484
Completeness, %	99.8	99.8	99.9	99.9
Reflections collected	4601	4700	6299	6039
Independent reflections	4107	3887	3283	3718
Goodness-of-fit on F^2	1.032	1.050	0.958	0.983
Final R indices [$I>2\sigma(I)$]	R1 = 0.0361	R1 = 0.0387	R1 = 0.0643	R1 = 0.0552
	wR2 = 0.0891	wR2 = 0.0908	wR2 = 0.1565	wR2 = 0.1344
Final R indices [all data]	R1 = 0.0408	R1 = 0.0497	R1 = 0.1166	R1 = 0.0908
	wR2 = 0.0924	wR2 = 0.0968	wR2 = 0.1833	wR2 = 0.1534

$R1 = \sum||Fo| - |Fc||/\sum|Fo|$ and $wR2 = |\sum w(|Fo|^2 - |Fc|^2)|/\sum|w(Fo)^2|^{1/2}$

Table S2. Selected bond lengths and angles for **1** and **2** at 120 K.

1		**2**	
Fe(1)-N(1)	2.1370(19)	Fe(1)-N(1)	2.147(2)
Fe(1)-N(2)	2.2571(14)	Fe(1)-N(2)	2.256(2)
Fe(1)-O(1)	2.1163(14)	Fe(1)-O(1)	2.095(2)
N(1)-Fe(1)-N(2)	90.97(6)	N(1)-Fe(1)-N(2)	91.18(8)
N(1)-Fe(1)-N(2)	89.03(6)	N(1)-Fe(1)-N(2)	88.81(8)
N(1)-Fe(1)-O(1)	88.77(7)	N(1)-Fe(1)-O(1)	88.38(9)
N(1)-Fe(1)-O(1)	91.23(7)	N(1)-Fe(1)-O(1)	91.62(9)
N(2)-Fe(1)-O(1)	85.58(6)	N(2)-Fe(1)-O(1)	94.01(8)
N(2)-Fe(1)-O(1)	94.42(6)	N(2)-Fe(1)-O(1)	85.99(8)
N(1)-Fe(1)-N(1)	180.00	N(1)-Fe(1)-N(1)	180.00
N(2)-Fe(1)-N(2)	180.0	N(2)-Fe(1)-N(2)	180.0
O(1)-Fe(1)-O(1)	180.0	O(1)-Fe(1)-O(1)	180.0
Fe(1)-N(1)-C(1)	171.28(16)	Fe(1)-N(1)-C(1)	171.7(2)
N(1)-C(1)-S(1)	179.10(19)	N(1)-C(1)-Se(1)	179.0(3)

Continuous Shape Measures (CShM) Analysis:

Continuous Shape Measures (CShM) analysis was carried out to determine the geometry around iron centers. Based on the values obtained, the idealized polyhedron was matched with the actual coordination spheres. The smallest value is symbolic of proximity of actual coordination sphere and idealized polyhedron.

Table S3. CShM analysis data for complexes **1** - **3**.

Complex	Structure				
	HP - 6	PPY - 6	**OC - 6**	TPR - 6	JPPY - 6
[Fe(**L1**)$_2$(NCS)$_2$(MeOH)$_2$] (**1**)	31.609	29.242	**0.193**	16.119	32.422
[Fe(**L1**)$_2$(NCSe)$_2$(MeOH)$_2$] (**2**)	31.690	29.166	**0.197**	16.103	32.276
[Fe(**L2**)$_2$(NCS)$_2$] (**3**) (**90 K**)	32.940	29.001	**0.043**	15.635	32.471
[Fe(**L2**)$_2$(NCS)$_2$] (**3**) (**200 K**)	32.848	28.427	**0.113**	15.691	31.703

HP – 6: Hexagon (D6h), PPY – 6 = Pentagonal pyramid, OC – 6: Octahedron (Oh), TPR – 6: Trigonal prism (D3h), JPPY – 6 = Johnson pentagonal pyramid J2 (C5v);

Octahedral Distortion Parameters

$\sum$ is the sum of the deviation from 90° of the 12 *cis*-angles of the FeN_4O_2 (**1** and **2**) / FeN_6 (**3**) octahedron; Θ is the sum of the deviation from 60° of the 24 trigonal angles of the projection of the FeN_4O_2 (**1** and **2**) / FeN_6 (**3**) octahedron onto the trigonal faces; ζ is the distance distortion parameter, which is the sum of deviation from individual Fe-N/O bond distances with respect to the mean metal-ligand bond distance.

Table S4 Selected hydrogen-bond parameters for **1** and **2** at 120 K.

	D-H···A	D-H / Å	H···A / Å	D···A / Å	∠D-H···A
1	O1-H1···N3	0.78(3)	1.89(3)	2.670(2)	174(3)°
2	O1-H1···N3	0.83(4)	1.84(4)	2.661(3)	173(4)°

Table S5. Selected bond lengths and angles for **3** at 90 K and 200 K.

	200	**90**
Fe(1)-N(1)	2.091(3)	1.949(2)
Fe(1)-N(2)	2.213(3)	1.996(2)
Fe(1)-N(3)	2.218(3)	2.007(2)
N(1)-Fe(1)-N(1)	177.35(16)	177.88(14)
N(1)-Fe(1)-N(2)	90.95(11)	89.16(10)
N(1)-Fe(1)-N(2)	90.92(11)	89.38(10)
N(1)-Fe(1)-N(3)	89.13(11)	90.17(10)
N(1)-Fe(1)-N(3)	89.05(10)	91.33(10)
N(2)-Fe(1)-N(2)	89.80(14)	92.24(14)
N(2)-Fe(1)-N(3)	178.42(10)	178.64(10)
N(2)-Fe(1)-N(3)	88.62(10)	88.93(10)
N(3)-Fe(1)-N(3)	92.96(14)	89.91(14)
Fe(1)-N(1)-C(1)	168.0(3)	170.3(2)
N(1)-C(1)-S(1)	178.5(4)	178.2(3)

References

1. S. Ghosh, S. Kamilya, T. Pramanik, M. Rouzieres, R. Herchel, S. Mehta and A. Mondal, *Inorg. Chem.*, 2020, **59**, 13009-13013.
2. Q.-F. Sun, J. Iwasa, D. Ogawa, Y. Ishido, S. Sato, T. Ozeki, Y. Sei, K. Yamaguchi and M. Fujita, *Science*, 2010, **328**, 1144-1147.
3. O. V. Dolomanov, L. J. Bourhis, R. J. Gildea, J. A. K. Howard and H. Puschmann, *J. Appl. Crystallogr.*, 2009, **42**, 339-341.
4. C. F. Macrae, P. R. Edgington, P. McCabe, E. Pidcock, G. P. Shields, R. Taylor, M. Towler and J. van de Streek, *J. Appl. Crystallogr.*, 2006, **39**, 453-457.
5. P. Gütlich, A. B. Gaspar and Y. Garcia, *Beilstein J. Org. Chem.*, 2013, **9**, 342-391.
6. C.-Y. Liu, H. Zhao and H.-h. Yu, *Org. Lett.*, 2011, **13**, 4068-4071.